Cell Reports

Article

Lamin A/C safeguards replication initiation by orchestrating chromatin accessibility and PCNA recruitment

Graphical abstract

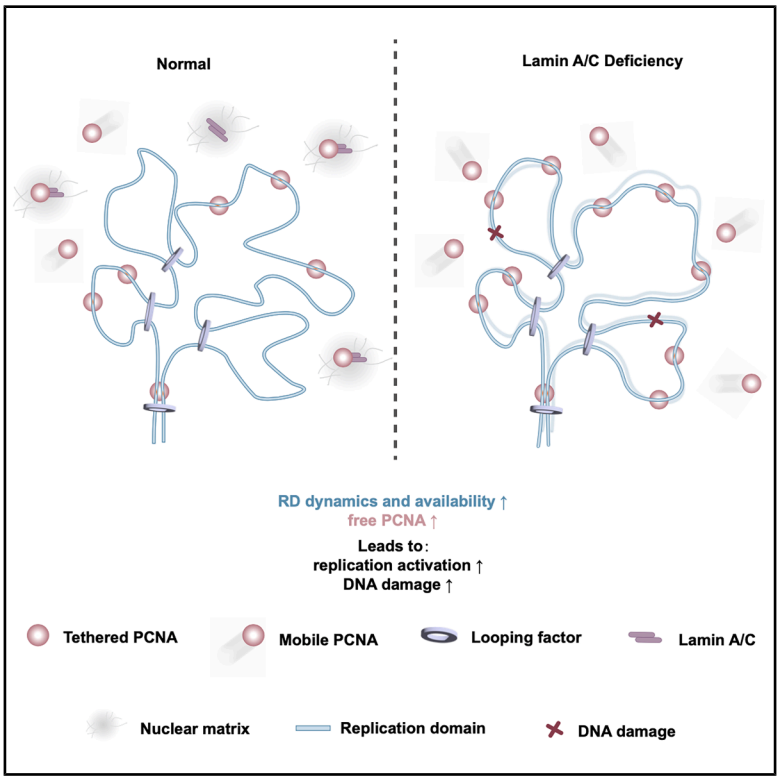

Highlights

- Super-resolution imaging reveals lamin A/C as a gatekeeper of early replication
- Excessive initiation events under lamin A/C loss trigger replication-dependent DNA damage
- Chromatin mobility and replication sites accessibility increase under lamin A/C deficiency
- Lamin A/C regulates PCNA availability and spatial distribution at replication domains

Authors

Mengling Zhang (张梦凌), Wenxue Zhao (赵文雪), Zhiguang Xiao (肖之光), ..., Dongyi Xu (徐冬一), Qian Peter Su (苏乾), Yujie Sun (孙育杰)

Correspondence

qian.su@uts.edu.au (Q.P.S.), sun_yujie@pku.edu.cn (Y.S.)

In brief

Zhang et al. reveal lamin A/C as a gatekeeper of replication initiation through effects on chromatin organization and PCNA availability in early S phase. Lamin A/C deficiency disrupts these controls, increasing initiation density and replication-dependent DNA damage.

Zhang et al., 2026, Cell Reports *45*, 117075
March 24, 2026
https://doi.org/10.1016/j.celrep.2026.117075

CellPress

Cell Reports

CellPress
OPEN ACCESS

Article

Lamin A/C safeguards replication initiation by orchestrating chromatin accessibility and PCNA recruitment

Mengling Zhang (张梦凌),[1,2,3,12] Wenxue Zhao (赵文雪),[4,12] Zhiguang Xiao (肖之光),[1,2,12] Lei Chang (常蕾),[5] Xiaotian Wang (王啸天),[2,3] Yichen Bai (柏亦陈),[6] Xiaodong Guan (管小东),[1,2,3] Tianyan Liu (刘天妍),[7] Zhaoru Zhang (张朝如),[1,2] Yongzheng Li (李永正),[8] Qing Li (李晴),[6,9] Cheng Li (李程),[4] Dongyi Xu (徐冬一),[6] Qian Peter Su (苏乾),[10,11,*] and Yujie Sun (孙育杰)[1,2,3,11,13,*]

[1]National Biomedical Imaging Center, College of Future Technology, Peking University, Beijing 100871, China
[2]State Key Laboratory of Membrane Biology & Biomedical Pioneering Innovation Center (BIOPIC), Peking University, Beijing 100871, China
[3]School of Life Sciences, Peking University, Beijing 100871, China
[4]School of Life Sciences, Center for Bioinformatics, Center for Statistical Science, Peking University, Beijing 100871, China
[5]Department of Cellular and Molecular Medicine, University of California, San Diego, La Jolla, CA, USA
[6]State Key Laboratory of Protein and Gene Research, School of Life Sciences, Peking University, Beijing 100871, China
[7]College of Future Technology, Institute of Molecular Medicine, National Biomedical Imaging Center, Beijing Key Laboratory of Cardiometabolic Molecular Medicine, Peking University, Beijing 100871, China
[8]Department of Pathogeny Biology, College of Basic Medical Sciences, Jilin University, Changchun 130021, China
[9]PKU-THU Center for Life Sciences, Peking University, Beijing 100871, China
[10]School of Biomedical Engineering, University of Technology Sydney, Sydney, NSW 2007, Australia
[11]Senior author
[12]These authors contributed equally
[13]Lead contact
*Correspondence: qian.su@uts.edu.au (Q.P.S.), sun_yujie@pku.edu.cn (Y.S.)
https://doi.org/10.1016/j.celrep.2026.117075

SUMMARY

Lamin A/C is essential for maintaining nuclear architecture, organizing chromatin, and preserving genomic stability. However, its role in regulating DNA replication remains unclear. This study investigates how lamin A/C regulates proper replication initiation by orchestrating the chromatin structure and the recruitment of proliferating cell nuclear antigen (PCNA). We demonstrate that lamin A/C deficiency leads to an increase in chromatin dynamics, replication domain (RD) accessibility, and PCNA availability at RDs, which together facilitate increased initiation density and replication-dependent DNA damage. These disruptions prolong the S phase and compromise genome stability, highlighting lamin A/C as a critical gatekeeper of balanced replication initiation. Our findings reveal lamin A/C's dual role in chromatin structure organization and replication machinery regulation, offering valuable insights into its involvement in replication-associated diseases and potential therapeutic opportunities.

INTRODUCTION

The precise regulation of DNA replication initiation is essential for maintaining genomic stability. Errors during replication can lead to replication stress, DNA damage, and genomic instability, which are hallmarks of cancer and other replication-associated diseases.[1,2] In mammalian cells, the replication of chromatin DNA begins at tens of thousands of potential replication origins. DNA replication initiation is tightly regulated by a two-step process, origin licensing and origin firing, which together ensure faithful duplication of the genome in both spatial and temporal dimensions.[3–7] During origin licensing, initiator proteins, including the origin recognition complex (ORC) and the minichromosome maintenance (MCM) complex, are sequentially assembled onto these potential origins, designating them for future activation. This is followed by origin firing, during which additional factors such as the Cdc45-MCM-GINS (CMG) helicase complex are recruited to a small subset (~10%) of these licensed origins, triggering the formation of bidirectional replication forks.[8,9] Origin firing then marks the onset of replication, driven by the assembly of the replisome machinery, including proliferating cell nuclear antigen (PCNA), a key factor for DNA synthesis and elongation.[10,11] The delicate regulation of this process is crucial, as both under- and over-activation of replication origins can disrupt the balance necessary for proper DNA replication. Insufficient activation of replication origins may compromise the completion of genome replication, while excessive origin activation can disrupt replication fidelity by inducing replication stress.[12–16] The complexity of replication regulation in higher eukaryotes is likely a consequence of their larger genomes and more intricate

chromatin organization, highlighting the need for robust spatiotemporal coordination to ensure genome stability.

Extensive studies have shown that DNA replication initiation is closely coordinated with the spatiotemporal organization of chromatin.[17–20] In metazoan cells, replication origins are not randomly distributed but are clustered within megabase (Mb)-sized chromosomal regions known as replication domains (RDs), which serve as functional units for coordinating replication initiation.[1,9] Each RD encompasses multiple replication origins, whose spatial positioning and activation patterns are regulated by factors such as chromatin accessibility, nuclear organization, and the local epigenetic landscape.[21] RDs replicate in a defined temporal order during the S phase, with replication timing correlating with the chromatin architecture. Chromatin architecture, defined by the hierarchical folding of the genome, consists of various structural elements, including nucleosomes, topologically associating domains (TADs), and higher-order compartments.[22–25] At the compartment level, transcriptionally active A compartments generally replicate earlier, while transcriptionally inactive B compartments replicate later.[23,26] TADs, which are conserved structural units of the genome, spanning ~0.5–1 Mb, help organize chromatin into functional domains.[24,27] The alignment of RD boundaries with TADs suggests that these chromatin structures function as units that orchestrate replication.[28] Advances in high-resolution imaging techniques, such as structured illumination microscopy (SIM),[29] stimulated emission depletion microscopy (STED),[30] stochastic optical reconstruction microscopy (STORM),[31–34] and expansion microscopy (ExM),[35,36] have provided unprecedented insights into the spatial organization of chromatin and its impact on DNA replication. These cutting-edge technologies allow for the precise visualization of RDs and their spatial organization at the nanometer scale, thereby enabling detailed single-cell investigations into how chromatin structure governs the spatiotemporal regulation of replication initiation.

In addition to chromatin architecture, nuclear scaffold proteins have also been suggested to play an important role in regulating DNA replication.[37–40] Lamin A/C, a key component of the nuclear lamina, maintains nuclear integrity and regulates chromatin dynamics.[41–44] Unlike B-type lamins, which preferentially remain anchored to the nuclear envelope due to permanent farnesylation, lamin A/C undergoes a transient farnesylation followed by proteolytic cleavage to produce its mature form.[45–48] Mature lamin A/C primarily localizes to the nuclear periphery, while a relatively dynamic and soluble pool remains in the nuclear interior.[49] Lamin A/C's unique dual distribution enables it to support nuclear architecture while simultaneously regulating chromatin structure and nuclear processes, with its deficiency being associated with increased chromatin dynamics,[50,51] altered chromatin structure,[52,53] replication stress,[47,54,55] and replication-related diseases such as cancer and viral infection.[46,56] Beyond its structural role in chromatin regulation, lamin A/C also interacts with PCNA,[57,58] suggesting a potential regulatory role in replication. Yet, the precise mechanism by which lamin A/C regulates DNA replication remains unclear, particularly whether its influence is exerted directly or mediated through chromatin organization. Our previous study identified a distinct chromatin-regulated spatial pattern of replication initiation and propagation, revealing that PCNA remains localized at the periphery of RDs from the G1 phase to the G1/S transition.[32,33] This positioning appears critical for the selective initiation of replication origins, potentially reflecting an interplay between PCNA and nuclear scaffold proteins such as lamin A/C. However, whether lamin A/C facilitates PCNA recruitment to RDs during replication initiation remains unclear, leaving the precise role of the lamin A/C-PCNA interaction in DNA replication to be further elucidated.

In this study, we investigate the multifaceted role of lamin A/C in regulating DNA replication initiation and maintaining genome stability. Utilizing super-resolution imaging methods combined with sequencing techniques, we revealed that lamin A/C acts as a gatekeeper, restricting the number of early replication sites. Lamin A/C deficiency alters the organization of RDs and increases PCNA recruitment to RDs. These changes collectively contribute to excessive initiation of early replication, resulting in elevated replication-dependent DNA damage. We propose a model in which lamin A/C simultaneously stabilizes the spatial structure of RDs and modulates PCNA expression as well as the proportion of freely diffusing PCNA, thereby maintaining a balanced early replication program and preventing excessive replication initiation. By elucidating lamin A/C's dual role in the regulation of chromatin organization and replication machinery, this study provides important insights into its critical function in preserving genome integrity.

RESULTS

Lamin A/C deficiency results in excessive replication initiation density and associated genome instability

To investigate the functional impact of lamin A/C, we utilized CRISPR-Cas9 to generate lamin A/C-deficient cell lines (HeLa S3 and MDA-MB-231). RNA sequencing (RNA-seq) followed by Kyoto Encyclopedia of Genes and Genomes (KEGG) pathway enrichment analysis revealed that lamin A/C deficiency led to differential expression of genes significantly enriched in pathways related to cancer and human papillomavirus (HPV) infection, both of which are associated with unscheduled DNA replication (Figures S1A and S1B). Additionally, Gene Ontology (GO) enrichment analysis showed that these differentially expressed genes were enriched in biological processes such as the cell cycle, cell proliferation, and DNA damage (Figures 1A and S1C). Specifically, E2F2 transcription factor (Table S1), which is a key regulator of DNA replication initiation and directly influences PCNA expression, was found enriched in these biological processes. Other key replication-related genes, such as the replication licensing factor CDC6 and replication stress response factor MCM8, were also enriched (Table S1). These findings suggest that lamin A/C may contribute to the coordination of DNA replication and the maintenance of genome integrity. However, its specific role in regulating replication initiation remains largely unexplored.

To investigate how lamin A/C influences replication initiation, we synchronized cells to the G1/S transition (STAR Methods; Figure S2A) and visualized early replication activity with a 10-min 5-ethynyl-2′-deoxyuridine (EdU) pulse upon release into S phase, which labels early replication sites representing early

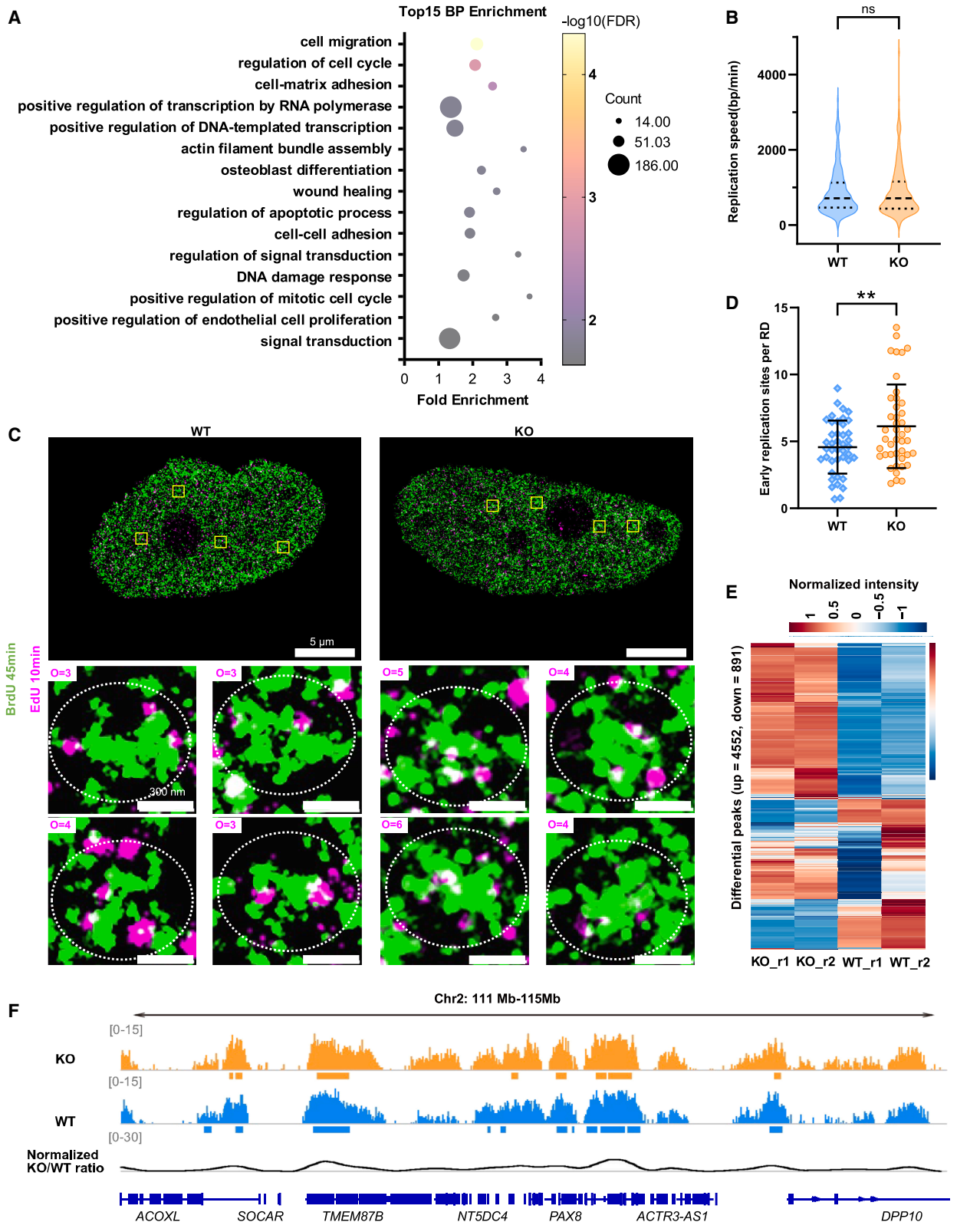

(legend on next page)

S phase synthesis events.[33,59] As indicated by the EdU-labeled early replication signal, early replication activity in lamin A/C-deficient cells was significantly increased compared to wild-type (WT) cells. This phenomenon was consistent across both HeLa and MDA-MB-231 cell lines (Figures S2B–S2E). Additionally, no EdU incorporation was detected prior to S phase release in either WT or lamin A/C-deficient cells (Figure S2C), excluding the possible effect of lamin A/C deficiency on cell synchronization. Consistently, moderate overexpression of lamin A/C in WT cells reduced the early replication signal in early S phase (Figure S3), indicating that lamin A/C dosage regulates early replication. The increased early replication signal upon lamin A/C deficiency reflects either an increase in the number of activated early replication sites or a change in replication fork speed.

Using DNA fiber assays, we first measured replication fork speed and found it unchanged between lamin A/C-deficient and WT cells (Figures 1B and S4A), arguing against a contribution of altered fork speed to the increased replication activity. To determine whether the elevated replication signals reflect an increase in the number of early activated replication sites, we quantified the inter-track distance after a 10-min pulse at early S phase, defined as the spacing between adjacent, clearly separated labeled tracks along the same DNA fiber (STAR Methods). Lamin A/C-deficient cells showed a significantly shorter inter-track distance than WT cells (Figure S4B), indicating a higher density of initiation events per unit length of DNA. To visualize this effect at the RD level, we performed dual labeling of early RDs and early replication sites, followed by STORM super-resolution microscopy with ~20 nm resolution.[31] Specifically, cells were first synchronized and released into S phase, during which bromodeoxyuridine (BrdU) was incorporated for 45 min to label early RDs. In the subsequent cell cycle, cells were re-synchronized at the G1/S transition and pulse-labeled with EdU for 10 min upon release to mark early replication sites. Individual BrdU-marked RDs and EdU-marked early replication sites were segmented using SR-Tesseler under identical parameters for WT and lamin A/C-deficient cells (Figure S5A; STAR Methods). RD areal density was comparable between WT and lamin A/C-deficient cells (~3 RDs per μm^2; Figure S5B), and their mean radius was ~100 nm, with only a mild increase in lamin A/C-deficient cells (Figure S5C). EdU-labeled early replication sites appeared as ~30 nm puncta, aligning with its spatial resolution and ensuring precise localization.[33] Notably, STORM-based quantification of RDs and early replication sites revealed a ~20% increase in the number of activated early replication sites per RD in lamin A/C-deficient cells (Figures 1C and 1D). Reintroduction of lamin A/C in lamin A/C-deficient cells reduced the number of early replication sites per RD to WT levels (Figure S6). These early replication sites were predominantly located at the RD periphery (Figure 1C), consistent with our previous findings.[33] Together, these data show that lamin A/C deficiency increases the number of activated early replication sites.

In addition to microscopy observation, we performed BrdU sequencing (BrdU-seq) to measure early replication activity in WT and lamin A/C-deficient cells during early 10-min S phase entry. Consistent with the imaging results, 83% of the 5,443 replication peaks exhibited increased peak heights in lamin A/C-deficient cells compared to WT cells (Figures 1E and S7A). The BrdU-seq peaks remained largely consistent with those in WT cells and were predominantly located within early RDs in A compartments, with no appreciable new peaks detected in mid or late-replicating regions (Figures 1F and S7B). Each BrdU-seq peak from the 10-min labeling typically spanned ~30–100 kb (Figure S7C), indicating that they represent clusters of multiple replication origins. This upregulation of replication peaks is consistent with the increased number of early replication sites observed by super-resolution microscopy (Figures 1C and 1D). Additionally, upregulated replication peaks were preferentially located near TAD boundaries compared to downregulated peaks (Figures S7D and S7E). These results confirm that the effect on early replication initiation by lamin A/C deficiency is primarily due to an increase in the number of early replication sites.

To rule out potential replication stress introduced by the aphidicolin-based synchronization method, which might activate dormant replication origins,[60,61] we adopted a mitotic shake-off-based synchronization method (STAR Methods; Figure S8A). Specifically, upon release from mitosis, cells were pulse-labeled with EdU for 8 h, followed by fixation and staining. Single-cell EdU fluorescence intensities were quantified and ordered to reflect cell cycle progression. The EdU signal exhibited a two-segment pattern: a near-flat segment corresponding to

Figure 1. Lamin A/C depletion leads to increased early replication

(A) Top 15 enriched GO biological process (BP) terms in HeLa cells. The bubble plot shows significantly enriched biological processes, with fold enrichment on the *x* axis, bubble size representing gene count, and color indicating $-\log_{10}$(FDR [false discovery rate]).

(B) Violin plot comparing replication fork speed between wild-type (WT, 194 forks) and knockout (KO, 204 forks) cells. Data represent median ± quartiles. ns, $p > 0.05$.

(C) Representative STORM images showing the distribution of RDs and early replication sites in WT (left) and lamin A/C KO (right) cells. Cells were synchronized, and RDs were labeled in early S phase with a 45-min BrdU pulse. After a second synchronization, early replication sites were labeled in early S phase with a 10-min EdU pulse. Scale bars, 5 μm. Below, enlarged rendered views of the yellow-boxed regions. Scale bars, 300 nm. The calculated number of early replication sites within each targeted RD (white circles) is indicated in the top-left corner of each magnified view.

(D) Quantification of early replication sites RD in WT and KO cells from the experiments in (C). Each dot represents the early replication sites per RD in a single cell. Data represent mean ± SE, with $n \geq 30$ cells. $^{**}p < 0.01$.

(E) Heatmap of differentially regulated BrdU-seq peaks (>10 kb). Heatmap displaying differentially regulated peaks of early S phase 10-min BrdU labeling, representing early replication signals, comparing WT and KO cells. Red indicates upregulated signals, while blue indicates downregulated signals. Data are derived from two independent replicates.

(F) BrdU-seq profiles at a representative genomic region on chromosome 2 (hg38, chr2: 111–115 Mb). BrdU-seq signal tracks for KO (top, orange) and WT (middle, blue) cells are shown together with peak calls (colored bars beneath each track). The lower track displays the normalized KO/WT signal ratio, highlighting regions with altered early replication. Gene annotations across this interval are shown below for reference.

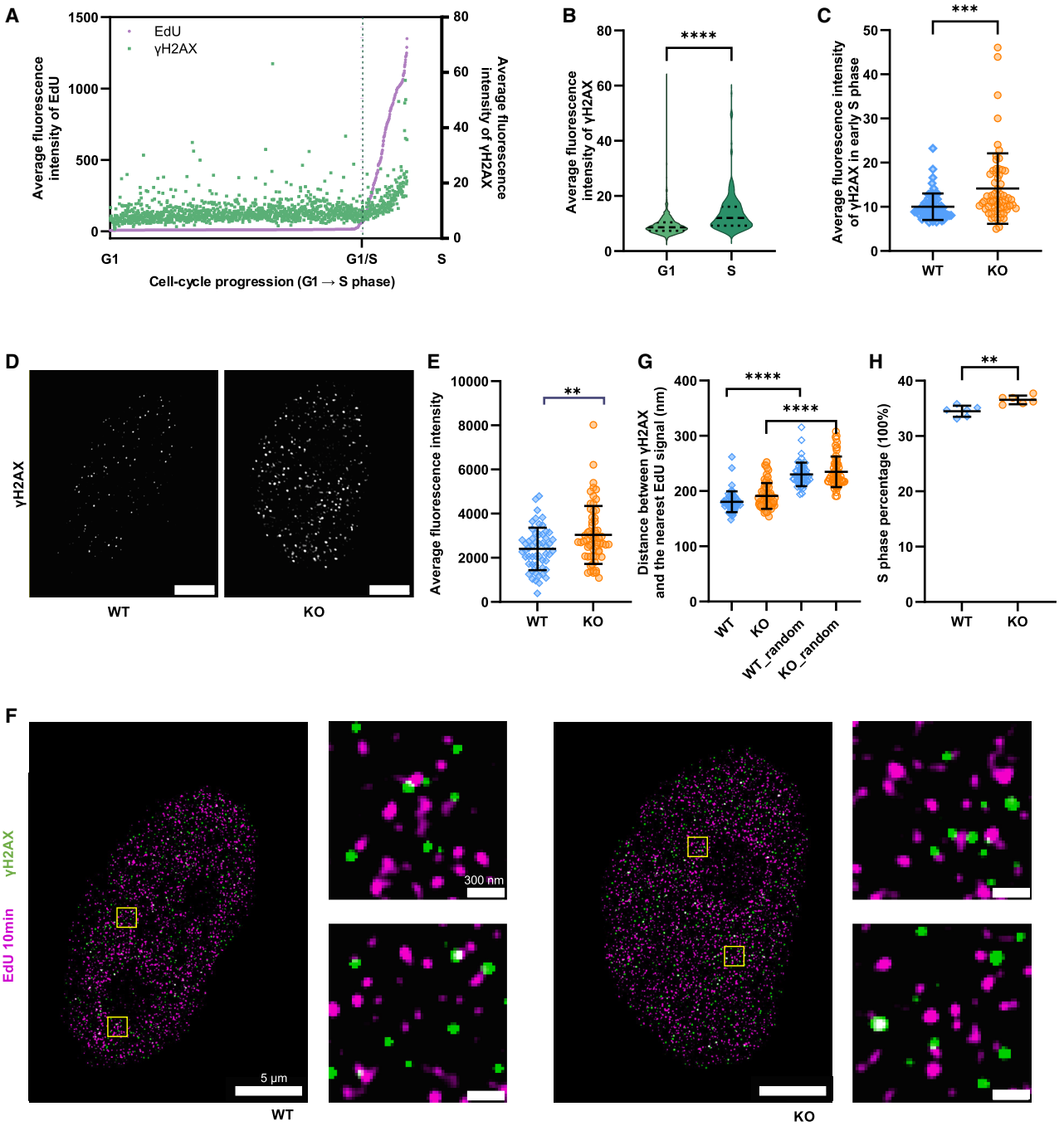

Figure 2. Replication-dependent damage in WT and lamin A/C KO cells

(A) Single-cell pseudo-time plot of EdU (purple, left axis) and γH2AX (green, right axis) fluorescence intensities in WT cells. Each dot represents an individual nucleus measured after a single fixation following mitotic shake-off and an EdU pulse (STAR Methods). Nuclei were rank-ordered by mean nuclear EdU intensity (low→high) to represent G1-to-S progression along the *x* axis. The purple dashed line marks the G1/S transition, identified by a two-segment piecewise linear fit to the EdU profile, and the green dashed line indicates the corresponding transition point for γH2AX determined by the same approach.

(B) The violin plot comparing γH2AX fluorescence intensity is in (A) before and after the G1/S transition. Data are shown as median ± quartiles. ****$p < 0.0001$.

(C) Quantification of average γH2AX fluorescence intensity in early S phase, measured after the G1/S transition as defined in (A), in WT and lamin A/C KO cells. Each dot represents the average γH2AX fluorescence intensity of a single cell.

(D) Representative images showing the distribution of γH2AX in WT (left) and KO (right) cells after 10 min of early S phase. Scale bars, 5 μm.

(E) Quantification of γH2AX fluorescence intensity in both cell types from the experiments in (D). Each dot represents the γH2AX fluorescence signal of a single cell ($n \geq 30$).

(legend continued on next page)

the G1 phase, followed by a sharply increasing segment indicative of S phase entry. The G1/S transition was defined as the inflection point between these two segments. Lamin A/C-deficient cells displayed a rapid increase in EdU signal following the G1/S transition and reached significantly higher EdU levels than WT cells, reflecting enhanced replication initiation during early S phase (Figure S4B). This finding is consistent with previous synchronization-based results and further supports the robustness of early replication signal detection.

Replication initiation is a tightly regulated process crucial for maintaining genomic stability. Both insufficient and excessive activation of replication origins can disrupt this balance, leading to replication-dependent DNA damage.[13,16] To investigate whether the increased replication initiation contributes to replication-dependent DNA damage, we performed the mitotic shake-off-based synchronization (STAR Methods; Figure S8A) on both WT and lamin A/C-deficient cells. Replication activity was measured by EdU incorporation, and DNA damage was assessed by γH2AX staining during the G1-to-S progression. Both EdU and γH2AX fluorescence intensity exhibited a two-phase pattern: a low, near-flat signal followed by a sharp increase. The inflection point of EdU incorporation, marking the G1/S transition, coincided with a marked increase in γH2AX signal (Figures 2A and S9A). γH2AX intensity was significantly higher after the inferred G1/S transition than before (Figures 2B and S9B), consistent with results obtained using the aphidicolin synchronization method (Figures S10A–S10D). These results indicate that the DNA damage increases at S-phase entry and reflects replication-dependent lesions. Additionally, γH2AX intensity was found modestly elevated in lamin A/C-deficient cells during G1 phase, possibly reflecting mechanical stress associated with lamin A/C deficiency (Figure S10E). Importantly, lamin A/C-deficient cells showed significantly higher γH2AX signals than WT cells after S phase entry (Figures 2C, S9C, and S10E), indicating an exacerbation of replication-dependent DNA damage. These findings were independently confirmed using aphidicolin synchronization (Figures 2D, 2E, and S10A–S10D). Furthermore, reintroduction of lamin A/C in lamin A/C-deficient cells partially reduced this replication-dependent DNA damage toward WT levels (Figure S11). Additionally, partially suppressing excessive early replication signal in lamin A/C-deficient cells by inhibiting DDK activity led to a measurable decrease in γH2AX signal (Figure S12), indicating that increased initiation activity contributes upstream to the DNA damage.

In parallel, the fluorescence intensity of phosphorylated RPA (pRPA), a marker of replication stress, was also found elevated in lamin A/C-deficient cells (Figures S10F and S10G). The spatial proximity of γH2AX with pRPA further supports replication stress as the source of DNA damage (Figures S10H and S10I).

To further investigate the spatial relationship between replication initiation and replication-dependent DNA damage, we performed dual-color super-resolution imaging of early replication sites and γH2AX. Both early replication sites (EdU 10-min pulse) and γH2AX signals appeared as punctate clusters in early S phase (Figure 2F). We quantitatively assessed their spatial proximity using nearest-neighbor distance (NND) analysis between EdU and γH2AX clusters. The sites of γH2AX were consistently found located near early replication sites in both WT and lamin A/C-deficient cells, with distances significantly smaller than the random distribution control (Figures 2F and 2G). This average distance of approximately 180 nm is close to the typical size of a TAD/RD,[33] suggesting a spatial association between replication-dependent DNA damage and initiation at the RD level.

These findings suggest that the increased number of early replication sites observed under lamin A/C deficiency enhances the likelihood of replication damage, highlighting a critical link between replication initiation density and genomic stability. Additionally, lamin A/C-deficient cells not only show a higher S phase fraction by flow cytometry (Figure 2H) but also display an overall longer cell cycle duration (Figure S13). These results together indicate that S phase duration is extended in the absence of lamin A/C, aligning with observations under lamin A/C knockdown in other cell lines.[62] While lamin A/C has been extensively implicated in maintaining replication fork stability and promoting DNA damage repair,[55,63,64] our results reveal an additional, upstream role in maintaining genome stability. By restricting the number of activated early replication sites, lamin A/C may reduce the risk of fork stalling and collapse, thereby maintaining the balance between replication initiation and DNA damage.

Lamin A/C deficiency affects RD structure and dynamics and increases replication sites' accessibility

Chromatin accessibility is closely associated with replication origin activation and has been implicated in influencing the spatial and temporal control of replication initiation.[21,65,66] To explore whether lamin A/C regulates replication initiation by modulating chromatin accessibility, we performed assay for transposase-accessible chromatin using sequencing (ATAC-seq) in both WT and lamin A/C-deficient cells. The results indicated increased accessibility within the A compartment (Figure S14A), where early RDs reside.[26] Integration of ATAC-seq and BrdU-seq data revealed increased chromatin accessibility at BrdU-defined early replication peaks in lamin A/C-deficient cells (Figure 3A). This accessibility gain is more pronounced at replication-associated peaks than at non-replicon ATAC peaks, which show only minimal changes (Figure S14B), suggesting that lamin A/C deficiency enhances replication sites' permissiveness by elevating chromatin accessibility.

(F) Representative STED images showing the spatial distribution of γH2AX (green) and early replication signals in WT (left) and lamin A/C KO (right) cells. Early replication signals are labeled with EdU (magenta) after 10 min of early S phase. Scale bars, 5 μm. Right, enlarged views of the regions highlighted by yellow boxes. Scale bars, 300 nm.

(G) Quantification of the nearest-neighbor distances (NNDs) between γH2AX and early replication signals from the experiments in (F). The control group shows the NND between γH2AX and EdU signals after randomizing the spatial distribution of γH2AX. Each dot represents the average NND measured in a single cell ($n \geq 30$).

(H) Flow cytometry analysis showing the proportion of cells in S phase for WT and KO cells, with 6 independent replicates (each dot represents one replicate). For (C), (E), (G), and (H), data represent mean ± SE. $^{**}p < 0.01$, $^{***}p < 0.001$, and $^{****}p < 0.0001$.

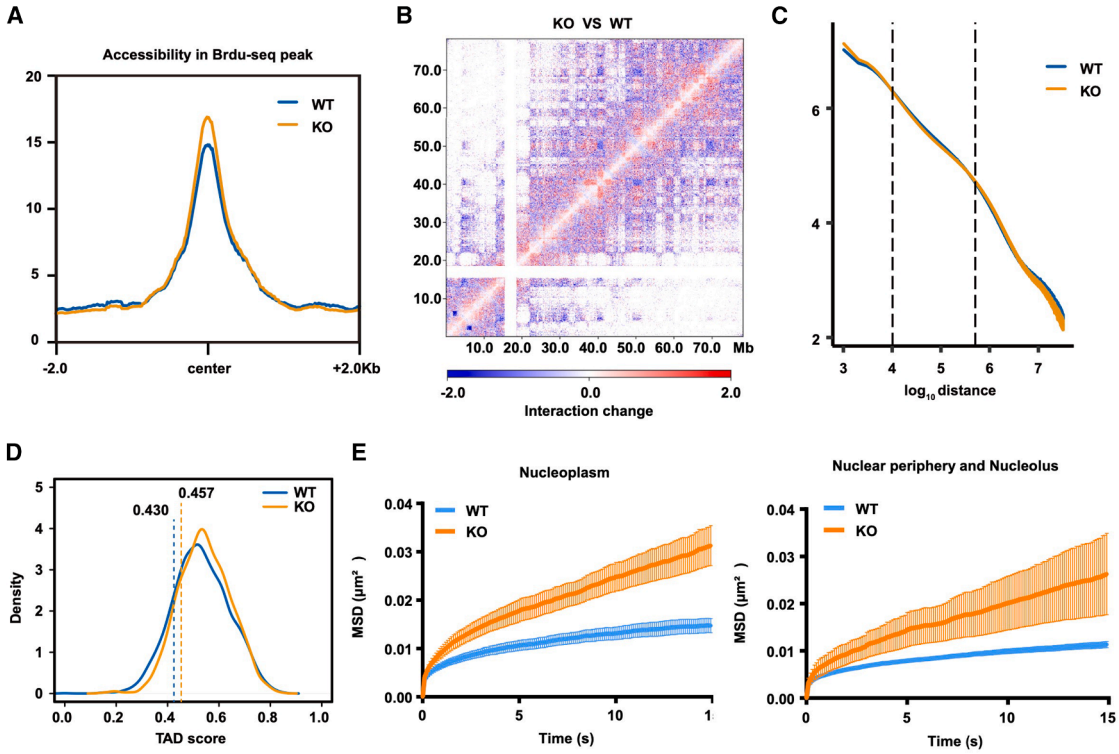

Figure 3. Regulation of chromatin dynamics and structure by lamin A/C depletion

(A) Chromatin accessibility at BrdU-seq peaks for WT (blue) and lamin A/C KO (orange) samples, 2 independent experiments.

(B) Difference map of Hi-C interaction frequencies for chromosome 18 (in megabases) between WT and KO cells, at a resolution of 100 kb. The color gradient from blue to red represents the change in chromatin interactions, with blue indicating a decrease and red indicating an increase in interactions.

(C) Hi-C interaction frequency as a function of increasing genomic distance (logarithmic scale) for WT and lamin A/C KO samples. Data are derived from two independent replicates. The vertical dashed lines mark ~10 kb and ~1 Mb. KO and WT curves show subtle but reproducible differences on both sides of this TAD-scale window, while overlapping closely within it.

(D) Distribution of TAD scores in WT and lamin A/C KO samples. TAD scores are calculated as shown in the schematic: TAD score = intra-TAD interactions/(intra-TAD + inter-TAD interactions). The vertical dash lines indicate the median values of each plot line. Wilcoxon test, $p < 0.01$.

(E) Averaged mean-squared-displacement (MSD) curves of three CRISPR-SunTag-labeled genomic loci tracked in WT and lamin A/C KO cells (>20 cells per locus; 3 independent experiments). The loci are located in distinct nuclear regions: one in the nucleoplasm (chr2: 1,218,818–1,227,201), one near the nuclear periphery (chr18: 13,673,058–13,676,522), and telomeric regions. Curves represent mean ± SEM.

To explore the structural basis of this accessibility change, we performed high-throughput chromosome conformation capture (Hi-C) analysis in both WT and lamin A/C-deficient cells (Figures S14C and S14D). Compartment analysis showed minimal A/B switching upon lamin A/C depletion (Figures S14E and S14F), and TAD boundaries remained largely conserved (Figures S14G and S14H), consistent with the unchanged replication timing observed by BrdU-seq (Figure S3B). However, we observed a mild reduction in long-range interactions and an increase in shorter-range (TAD-scale) interactions (Figures 3B and 3C), and the distribution of the TAD interaction score (intra-TAD/[intra-TAD + inter-TAD]) was right-shifted in lamin A/C-deficient cells (Figure 3D). These findings suggest that lamin A/C depletion leaves compartments and TAD boundaries largely intact, but is associated with modest but significant reorganization of contact patterns within TADs/RDs.

Chromatin mobility has been linked to both structural organization and replication efficiency.[33,67,68] To assess whether the observed architectural changes are accompanied by altered chromatin dynamics, we performed single-molecule tracking of three CRISPR-SunTag-labeled genomic loci: (1) near the nuclear periphery, (2) within the nuclear interior, and (3) containing telomeres (STAR Methods; Figure S15A). All three loci exhibited increased mobility under lamin A/C deficiency (Figures 3E and S15B), indicating globally enhanced chromatin dynamics.

These findings indicate that lamin A/C deficiency increases chromatin accessibility at early replication sites, accompanied by local structural reorganization and increased chromatin dynamics. These combined changes contribute to a more permissive environment for early replication.

Lamin A/C regulates replication initiation by interacting with PCNA

Previous studies revealed that PCNA interacts specifically with the Ig-fold domain of lamin A/C at the C terminus, and disrupting this interaction induces replication stress.[57,58] Accordingly, analysis of lamin A/C interaction data from the BioGRID database[69] also identified PCNA as a robust interacting partner of lamin

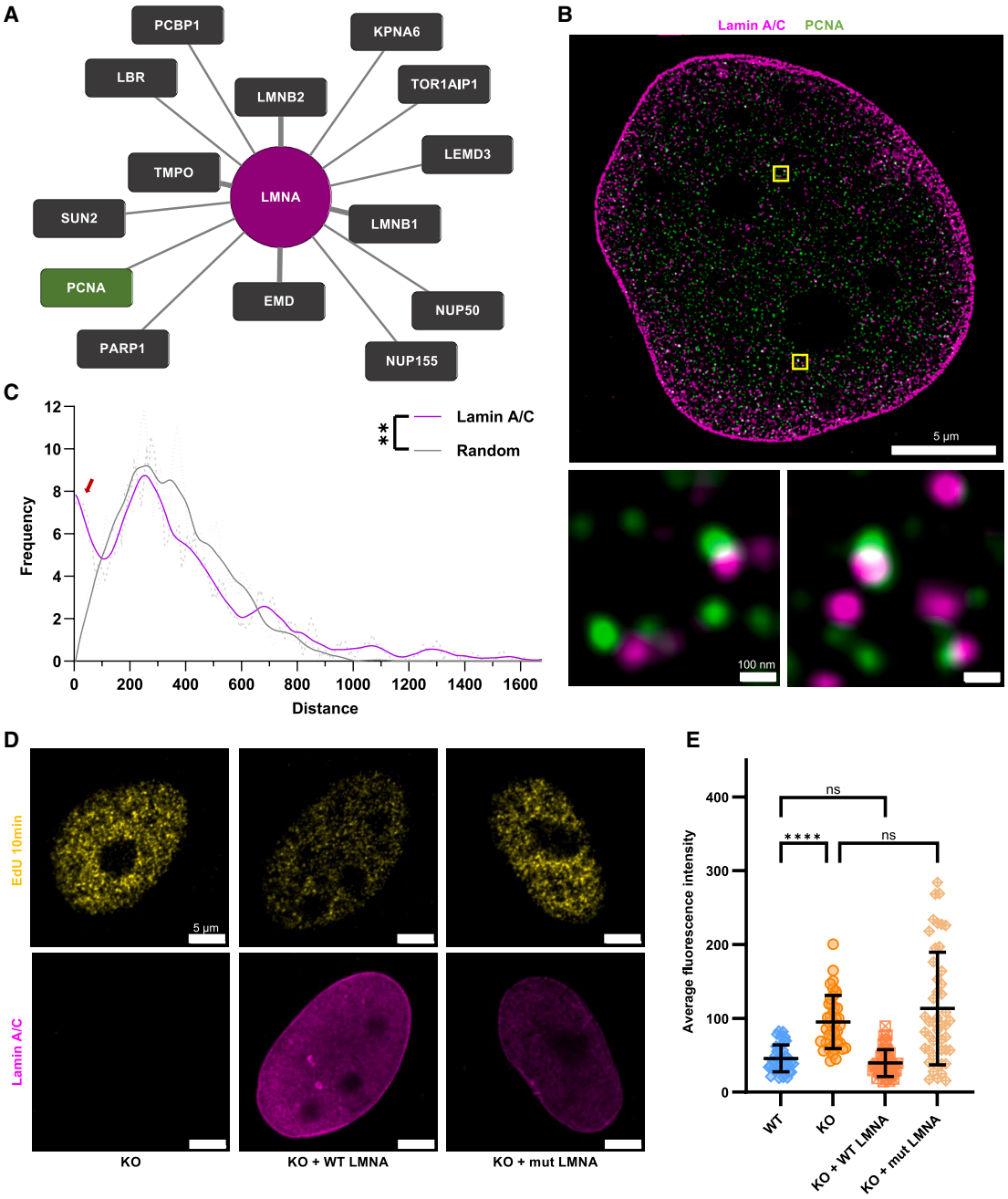

Figure 4. Interaction between lamin A/C and PCNA regulates replication initiation

(A) Visualization of a selected interaction network of proteins identified in proximity to lamin A/C (magenta), showing only proteins with an interaction evidence score greater than 8 (according to BioGRID and Figure S16). PCNA is highlighted in green, as indicated in the figure key, to emphasize its role in the network. The other associated genes from the same organism (dark gray). Thicker connection lines (gray) represent stronger evidence supporting the interactions.

(B) STED microscopy image showing the spatial distribution of lamin A/C (magenta) and PCNA (green) at the G1/S transition. Top: nuclear view. Scale bars, 5 μm. Bottom: magnified views of the regions highlighted by yellow boxes. Scale bars, 100 nm.

(C) Frequency distribution of the nearest-neighbor distances between PCNA and lamin A/C in non-perinuclear regions, based on the analysis in (B). The *x* axis shows nearest-neighbor distances, and the *y* axis shows frequency. The control represents randomized lamin A/C distribution in non-perinuclear regions. Dashed lines show raw data, solid lines show lowess smoothed trends, and red arrows mark peaks of a notable subset in the experimental group. Data are based on more than 20 cells. $^{**}p < 0.01$.

(D) Representative images showing the distribution of early replication signals in lamin A/C KO cells (left), lamin A/C WT rescue cells (middle), and lamin A/C mutant rescue cells (right). After synchronization, cells were labeled with EdU for 10 min during early S phase. Scale bars, 5 μm.

(E) Quantification of EdU fluorescence intensity per unit nuclear area from the experiments in (D). Each dot represents the mean nuclear EdU intensity measured in a single cell. Data represent mean ± SE, with $n \geq 30$ cells. ns, $p > 0.05$ and $^{****}p < 0.0001$.

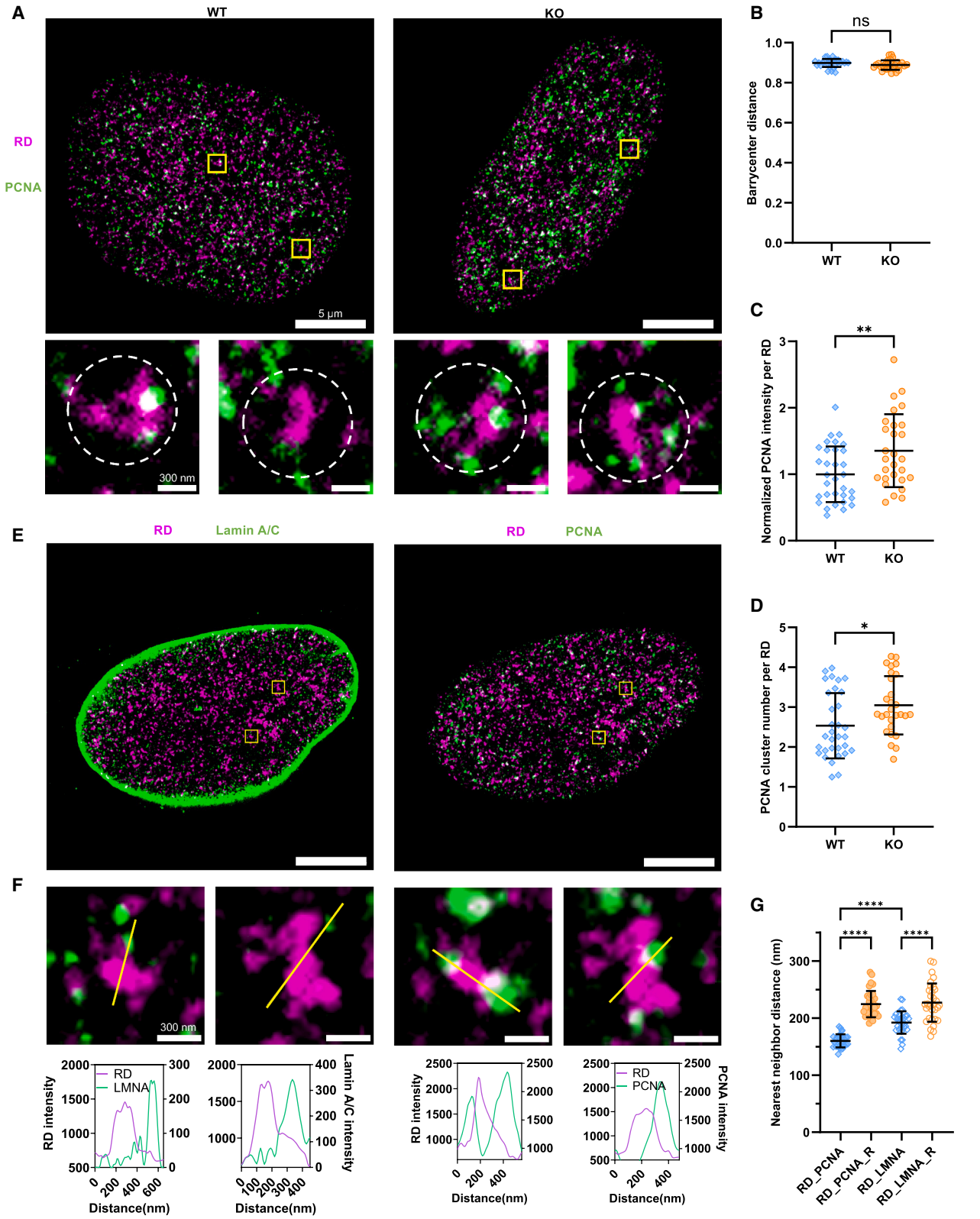

(legend on next page)

A/C (Figures 4A and S16). To investigate how this interaction regulates DNA replication initiation, we employed super-resolution microscopy to examine the spatial distribution of lamin A/C and PCNA during the G1/S transition. Both PCNA and lamin A/C were observed as punctate clusters within the nuclear interior (Figure 4B). Interestingly, by calculating the NND between PCNA and lamin A/C, we identified two distinct populations of lamin A/C clusters within the nuclear interior, in contrast to a randomized lamin A/C distribution control. The majority were located 200 to 400 nm away from PCNA, exhibiting a distribution consistent with random chance, which suggests that these clusters may serve PCNA-independent functions. However, a notable subset, representing 14.3% of the lamin A/C clusters, was found in close proximity to PCNA, at distances of less than 100 nm (Figures 4B and 4C). Expanding on the previous reports,[58] the proximity between lamin A/C and PCNA suggests a regulatory role for their interaction in controlling early replication synthesis at the onset of DNA replication.

To further elucidate the role of the interaction between PCNA and lamin A/C during early replication, we conducted rescue experiments in lamin A/C-deficient cells by expressing either WT lamin A/C or lamin A/C Ig-fold deletion mutant, lacking the interaction with PCNA. Reintroducing WT lamin A/C restored early replication activity to WT levels (Figures 4D and 4E). In contrast, the reintroduction of the lamin A/C Ig-fold deletion mutant failed to rescue the phenotype and showed early replication signals comparable to lamin A/C-deficient cells; both conditions were significantly higher than WT levels (Figures 4D and 4E).

To directly assess how the Ig-fold deletion affects PCNA tethering, we quantified the NND between PCNA and lamin A/C. In cells expressing the Ig-fold mutant, the PCNA-lamin A/C distance distribution peaked at ~200 nm and overlapped with randomized controls (Figure S17), indicating a loss of PCNA enrichment in the vicinity of lamin A/C. These findings highlight that the interaction between lamin A/C and PCNA is required for proper regulation of early replication synthesis and the maintenance of genome stability.

Lamin A/C deficiency increases PCNA recruitment to replication domains

Our previous study showed that PCNA sites are maintained at the periphery of RDs from G1 to G1/S phase, suggesting that its positioning is crucial for replication initiation.[33] Given this, we hypothesized that lamin A/C deficiency might alter the spatial distribution of PCNA. To test this hypothesis, we followed a labeling and analysis protocol based on our previous work (STAR Methods). Briefly, cells were first synchronized and released into the S phase, with EdU incorporated for 45 min to label early replicating domains. In the subsequent cell cycle, the cells were re-arrested at the G1/S transition and labeled for both EdU and PCNA. ExM was then used to image the labeled cells, and the spatial distribution of PCNA relative to RDs was quantified using the barycenter distance distribution (BDD) calculation,[33] defined as the physical distance between the barycenter of an RD and the barycenter of PCNA, normalized by the radius of gyration of the RD.

Expanding on our prior findings,[33] we confirm that PCNA was primarily located at the periphery of RDs in WT cells during the G1/S transition (Figures 5A and 5B). This spatial organization remained largely unchanged in lamin A/C-deficient cells, with BDD values both close to 1. However, further analysis revealed that lamin A/C deficiency influenced the enrichment of PCNA near RDs. Specifically, we observed an increase in the number of PCNA clusters and an overall increase in PCNA fluorescence intensity near RDs under lamin A/C deficiency (Figures 5C and 5D). To determine whether these PCNA signals correspond to active replication, we performed a 10-min EdU pulse at early S phase and quantified the spatial proximity between EdU-labeled early replication sites and PCNA. The NND between EdU and PCNA signals was strongly shifted toward short distances compared with a randomized control, with a median below 100 nm (Figure S18). This indicates that the majority of PCNA puncta we detect are closely associated with ongoing replication activity. These observations support the view that lamin A/C loss increases PCNA accumulation at replication-associated regions. Additionally, to further validate these observations, we conducted cleavage under targets and tagmentation (CUT&Tag)[70] experiments (STAR Methods) and demonstrated a significant enhancement of PCNA enrichment on chromatin in lamin A/C-deficient cells (Figure S19). These spatial observations were independently validated by STED microscopy, with consistent results across biological replicates (Figure S20). Collectively, these results suggest that lamin A/C deficiency increases PCNA enrichment at early replication sites, thereby supporting the formation of additional initial replication forks and contributing to enhanced early replication.

Figure 5. Spatial distribution of RDs, PCNA, and lamin A/C in WT and lamin A/C KO cells

(A) Representative ExM images showing the spatial distribution of PCNA (green) and RD (magenta) in WT (left) and Lamin A/C KO (right) cells. Scale bars, 5 μm. Below: enlarged rendered views of the regions highlighted by yellow boxes, and the white circle indicates the target RDs. Scale bars, 300 nm.

(B) Dot plot quantifying the normalized barycenter distances between the centers of PCNA and RD in WT and lamin A/C KO cells from the experiments in (A). The BDD value by random simulations was 0.71.[33]

(C) Dot plot quantifying the total PCNA fluorescence intensity near the RD (within 1.5 times the radius of gyration of the RD) in WT and lamin A/C KO cells from the experiments in (A).

(D) Dot plot showing the number of PCNA clusters near the RD (within 1.5 times the radius of gyration of the RD) in WT and lamin A/C KO cells from the experiments in (A).

(E) Representative ExM images showing the spatial distribution of RD (magenta) with lamin A/C (green, left) or PCNA (green, right) in WT cells. Scale bars, 5 μm.

(F) Enlarged rendered views of the yellow-boxed regions in (E). Left: the distribution of RD (magenta) and lamin A/C (green). Right: the distribution of RD (magenta) and PCNA (green). Bottom: fluorescence intensity line profiles along the yellow line.

(G) Dot plot quantifying the nearest-neighbor distances between the centroids of RD and PCNA or lamin A/C clusters from the experiments in (E). The random group represents the nearest-neighbor distances between RD and randomly distributed PCNA or lamin A/C clusters. For (B), (C), (D), and (G), data represent mean ± SE, with each dot representing a cell ($n \geq 30$). ns, $p > 0.05$; *$p < 0.05$; **$p < 0.01$; and ****$p < 0.0001$.

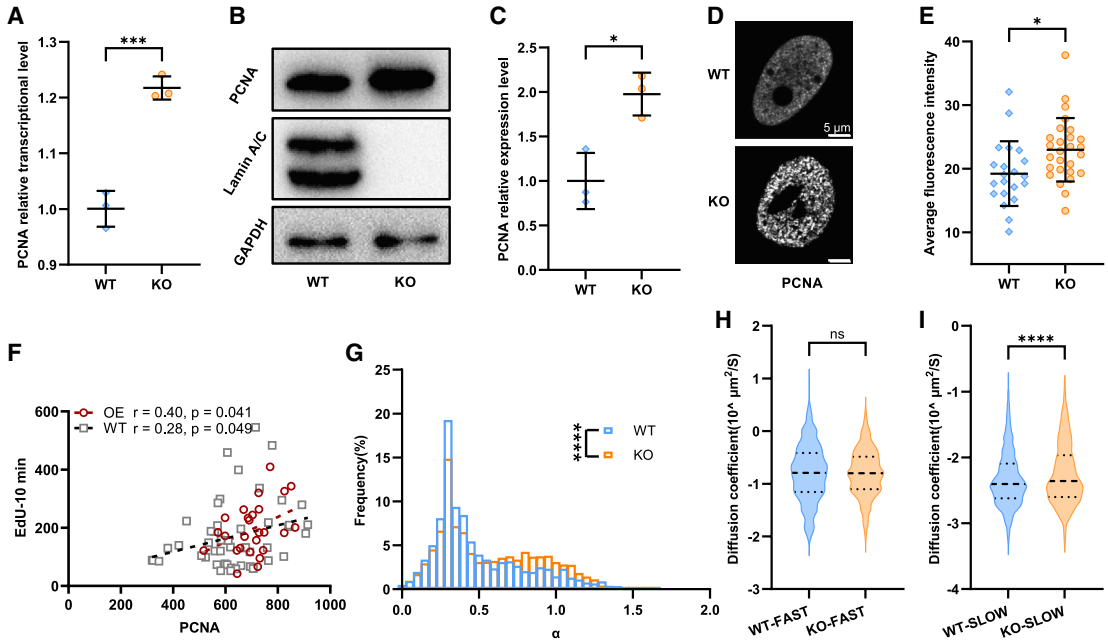

Figure 6. Impact of lamin A/C depletion on PCNA dynamics and expression

(A) Quantification of relative PCNA transcriptional levels in WT and lamin A/C KO cells using reverse transcription quantitative PCR (RT-qPCR) (3 replicates).

(B) Representative immunoblot showing PCNA expression levels in WT and lamin A/C KO cells.

(C) Quantification of relative PCNA protein levels from the experiments in (B) (3 replicates).

(D) Representative images showing the nuclear distribution of PCNA at the G1/S transition in WT (top) and lamin A/C KO (bottom) cells. Scale bars, 5 μm.

(E) Quantification of nuclear PCNA fluorescence intensity per unit area from the experiments in (D), with each dot representing the average PCNA fluorescence intensity measured in a single cell ($n > 20$).

(F) Scatterplot showing the correlation between the mean fluorescence intensity of PCNA and 10-min EdU labeling signals in WT (black) and PCNA overexpression cells (red). Each dot represents the average fluorescence measured in a single cell. Statistical significance was evaluated by correlation analysis. The dashed line shows the trend calculated by a simple regression model.

(G) Frequency histogram plot of the anomalous diffusion index (α) for PCNA molecules during the G1/S transition in both cell types.

(H) Violin plot showing the diffusion coefficients of free PCNA molecules ($\alpha \geq 0.7$) at the G1/S transition in both cell types.

(I) Violin plot showing the diffusion coefficients of DNA-bound PCNA molecules ($\alpha < 0.7$) at the G1/S transition in both cell types. For (A), (C), and (E), data represent mean ± SE. For (H) and (I), data are shown as median ± quartiles. For (G)–(I), data are from more than 7 cells. For (A), (C), (E), (H), and (I), ns, $p > 0.05$; *$p < 0.05$; ***$p < 0.001$; and ****$p < 0.0001$.

To further examine how lamin A/C is spatially related to RDs and PCNA, we conducted simultaneous imaging of these three components at the G1/S transition. The NND analysis revealed that both lamin A/C and PCNA were in close spatial proximity to RDs (Figures 5E–5G). This supports the notion that lamin A/C is partly associated with RDs and may help maintain their higher-order architecture (Figure 3). In parallel, PCNA was located approximately 40 nm closer to RDs than lamin A/C, consistent with PCNA's direct engagement in DNA replication, whereas lamin A/C likely acts as a structural scaffold. The observed spatial organization complements the enrichment analyses of PCNA (Figures 5A–5D) and supports a model in which lamin A/C contributes to the structural organization of RDs.

Lamin A/C regulates PCNA expression and available portion

Previous studies have shown that the Lap2α-Lamin A/C complex regulates PCNA expression by modulating pRb and E2F1 activity,[71,72] suggesting that lamin A/C influences PCNA expression. To assess this, we first quantified PCNA expression at both the RNA and protein levels and observed a significant elevation in lamin A/C-deficient compared to WT cells (Figures 6A–6C). We also observed elevated PCNA immunofluorescence intensity during the G1/S transition, coinciding with increased early replication signal (Figures 6D and 6E). These findings provide additional evidence supporting the regulatory role of lamin A/C in PCNA expression. Furthermore, fluorescence intensity analysis revealed a positive correlation between PCNA levels and 10 min EdU incorporation, linking PCNA upregulation to early replication (Figure 6F). Consistently, partial reduction of PCNA in lamin A/C-deficient cells decreased the early replication signal toward WT levels (Figure S21), indicating that PCNA abundance contributes to the elevated replication activity in the absence of lamin A/C. Beyond controlling expression, lamin A/C also acts as an immobile nuclear scaffold protein that physically interacts with PCNA. This interaction raises the possibility that lamin A/C sequesters free PCNA molecules within the nucleus and regulates their availability to early replication sites. To evaluate this, we generated stable cell lines expressing HaloTag-fused PCNA in both WT and lamin A/C-deficient cells. The mobility of

single PCNA molecules at the G1/S transition was tracked in real-time (Figure S22) with HaloTag, which is a modified dehalogenase that binds to ligands conjugated with fluorescent dyes and enables precise live-cell protein tracking.[73] Single-particle tracking of PCNA molecules allowed us to quantify their motion during the G1/S transition. Analysis of the anomalous diffusion exponent (α) revealed two mobility states: a DNA-bound population ($\alpha < 0.7$) and a freely diffusing population ($\alpha \geq 0.7$). Lamin A/C deficiency led to a higher proportion of freely diffusing PCNA (Figure 6G), indicating an enlarged pool of unbound PCNA available for recruitment. Because total PCNA expression is also elevated (Figure 6F), both the freely diffusing and DNA-bound populations increased in absolute abundance. The absolute amount of DNA-bound PCNA revealed a ~1.6-fold increase in lamin A/C-deficient cells compared to WT cells, in line with the enhanced PCNA enrichment toward RDs (Figure 5C). These findings highlight that lamin A/C deficiency increases both the pool of freely diffusing PCNA and the absolute amount of DNA-bound PCNA, which is consistent with greater PCNA availability for recruitment to early replication sites in early S phase.

We next analyzed the diffusion coefficient (D) as a measure of mobility within each population. The mobility of freely diffusing PCNA remained comparable between WT and KO cells (Figure 6H), whereas the DNA-bound population exhibited a modest but significant increase in mobility (Figure 6I). This elevated mobility likely reflects a more dynamic chromatin environment in lamin A/C-deficient nuclei, consistent with the increased chromatin dynamics (Figure 3).

Collectively, our data show that lamin A/C deficiency is accompanied by higher PCNA abundance and a larger mobile PCNA fraction in early S phase. These observations, together with increased early replication synthesis, are consistent with a model in which lamin A/C acts as a spatial buffer that limits the pool of freely available PCNA and thereby modulates its effective availability at replication sites.

DISCUSSION

Our study reveals that lamin A/C regulates DNA replication initiation and genome stability. Specifically, lamin A/C deficiency led to an increased number of activated replication sites in the early S phase (Figure 1), which is accompanied by increased replication-dependent DNA damage and genomic instability (Figure 2). These phenotypes are linked to accelerated chromatin dynamics and reorganized chromatin architecture, including altered domain-level interactions and increased accessibility at RDs (Figure 3). Moreover, the direct interaction between lamin A/C and PCNA via the Ig-fold domain regulates replication initiation (Figure 4). Super-resolution imaging revealed increased PCNA enrichment at RD boundaries (Figure 5), which is supported by elevated PCNA expression and a higher proportion of freely diffusing PCNA molecules under lamin A/C deficiency (Figure 6). Together, these findings support a two-pronged model in which lamin A/C acts as a spatial gatekeeper to limit excessive replication and preserve genomic integrity by restricting chromatin movement to stabilize RD organization and limit replication site accessibility, and by modulating PCNA availability through direct sequestration and suppression of expression.

Prior studies have established that replication origin licensing is achieved during the G1 phase by ORC-mediated loading of the MCM2-7 helicase to prepare origins for replication activation in S phase,[8,9] while ATR-Chk1 checkpoint suppresses unscheduled origin firing, especially under replication stress.[74,75] These canonical pathways govern both the timing and efficiency of replication origin activation. In parallel, our findings reveal that lamin A/C limits early replication initiation density, without markedly influencing replication timing (Figures 1F and S3B). Beyond the canonical mechanism, lamin A/C may regulate replication initiation through structural constraints on both chromatin and the spatial enrichment of PCNA.

First, these structural constraints build upon prior studies extensively demonstrating lamin A/C's architectural roles in organizing nuclear compartments.[50,51,53] Prior work has laid the foundation for understanding how lamin loss disrupts chromatin architecture by altering TAD interactions and detaching LADs (lamin-associated domains) from the nuclear lamina.[53] Lamin A/C deficiency has also been reported to be associated with increased chromatin accessibility across broad genomic regions.[76] Extending these observations, our results not only confirmed the reorganization of higher-order chromatin domains but also revealed increased chromatin accessibility preferentially at replication initiation zones (Figure 3C), suggesting that lamin A/C-mediated nuclear architecture may contribute structurally to replication initiation control. Although our study does not address potential compensatory effects from other lamins, the observed chromatin changes in lamin A/C-deficient cells support a model in which lamin A/C constrains replication initiation by maintaining the integrity and stability of RDs.

Second, these structural constraints are complemented by the previously described Lap2α-lamin A/C complex, which regulates PCNA expression through the pRb-E2F axis.[71,72] In addition to this transcriptional regulation, lamin A/C also exerts direct spatial control by constraining PCNA diffusion (Figure 6G). Although PCNA, unlike canonical initiation regulators (e.g., CDC45/GINS1),[14,77] acts downstream of origin licensing and firing, it is essential for replisome progression.[10,11] Accordingly, its local enrichment can provide a permissive environment for replisome assembly at the onset of S phase. Consistently, our data suggest that lamin A/C-mediated PCNA tethering may buffer PCNA availability and contribute an additional layer of spatial control over DNA replication initiation density.

In summary, our study integrates super-resolution microscopy, single-molecule tracking, and genome sequencing to dissect how early replication sites are spatially organized and regulated. By directly visualizing the number of replication sites (Figure 1C), PCNA distribution (Figure 5A), and the spatial relationship between early replication and DNA damage (Figure 2F), our results support a model of lamin A/C's regulation of replication initiation. These findings have broader implications for understanding how nuclear structure contributes to genome stability in both physiological and pathological contexts. For example, lamin A/C is frequently downregulated or mutated in laminopathies and cancers,[46,56] and such alterations are associated with increased DNA damage and genomic instability. Our findings suggest that lamin A/C regulates replication initiation and that its deficiency may lead to increased replication-associated genome instability.

This regulatory pathway may provide a mechanistic link between lamin A/C dysfunction and tumorigenesis. Moreover, some viruses, such as HPV, have been reported to downregulate lamin A/C,[56] potentially creating a more permissive replication environment. The prolonged S phase observed under lamin A/C deficiency in our study may further facilitate viral genome integration and replication.

Limitations of the study

While our study reveals correlations among lamin A/C deficiency, increased RD accessibility, elevated PCNA availability, enhanced early replication, and increased DNA damage, the causal order of these events cannot be definitively established from our mainly steady-state analyses. Temporally resolved analyses and acute depletion approaches would be needed to delineate the causal hierarchy among these phenotypes. Additionally, while the lamin A/C Ig-fold domain appears critical for restraining replication initiation, it mediates other protein interactions, and our current data cannot exclude additional PCNA-independent functions. Thus, the specific contribution of the lamin A/C-PCNA interaction to the observed phenotypes remains only partially resolved. We were also not able to perform a clean gain-of-function test of PCNA sufficiency: constitutive overexpression perturbs cell-cycle homeostasis and genome stability.[78,79] Inducible, titratable systems will be required to evaluate PCNA dosage effects in a physiologically relevant manner.

Beyond PCNA, we did not determine whether lamin A/C also regulates other replication factors, such as the MCM complex. Moreover, PCNA loading and unloading are regulated by RFC and ATAD5/Elg1 complexes,[10,80,81] and potential interfaces between lamin A/C and these pathways were not addressed here. Finally, all experiments were performed in cultured cell lines; we did not investigate lamin A/C-mediated replication control in primary tissues or *in vivo*. As a result, the physiological and pathological relevance of this mechanism in development, cancer, and viral infection remains to be established.

RESOURCE AVAILABILITY

Lead contact

Further information and requests for resources and reagents should be directed to the lead contact, Yujie Sun (sun_yujie@pku.edu.cn).

Materials availability

All unique/stable reagents generated are available from the lead contact without restriction.

Data and code availability

- High-throughput sequencing datasets generated (RNA-seq, BrdU-seq, ATAC-seq, CUT&Tag, and Hi-C) have been deposited at GEO and are publicly available as of the date of publication under accession numbers GEO: GSE289473, GSE289474, and GSE289475. Additional analysis data and code can be obtained by contacting the corresponding author.
- Microscopy datasets (including super-resolution images, DNA fiber images, and single-molecule tracking movies), as well as processed numerical data underlying the main figures and supplemental figures, will be shared by the lead contact upon request.
- Any additional information required to reanalyze the data reported in this paper is available from the lead contact upon request.

ACKNOWLEDGMENTS

We appreciate Dr. Daochun Kong and Dr. Fei Wu for their guidance on DNA fiber experiments. We thank Dr. Huiwen Hao for her valuable suggestions on imaging experiments. We are grateful to Dr. Wu Honggui of Xiaoliang Xie Laboratory for technical advice on BrdU-seq experiments. We acknowledge the Fenghuang Imaging Platform (Dr. Chunyan Shan, Dr. Siyin Qin, Dr. Yinghua Guo, and Dr. Liqin Fu) for providing instrument support.

This work is supported by the National Natural Science Foundation of China (22127804 to Y.S.), the National Key R&D Program of China (2022YFA1303103 and 2022YFA3401100 to Y.S.), and the Australian National Health and Medical Research Council (Emerging Leadership APP1177374 and APP2041674 to Q.P.S.).

AUTHOR CONTRIBUTIONS

M.Z., Y.S., and Y.L. conceptualized the research problem. M.Z. and Y.S. designed the experiments. M.Z. completed all super-resolution imaging; PCNA single-molecule tracking imaging; parts of confocal imaging; and experiments for BrdU-seq, CUT&Tag, and RNA-seq and also led the experimental data analysis. W.Z. analyzed the sequencing data, including BrdU-seq, Hi-C, and CUT&Tag. Z.X. contributed to STORM imaging, the construction of MDA-MB-231 KO cell lines, lamin A/C complementation experiments, and imaging experiments related to DNA damage. L.C. performed the Hi-C and chromatin loci tracking experiments. X.W. provided the original code for image analysis. Y.B. carried out the DNA fiber experiments. X.G. built the STORM imaging system. T.L. provided technical guidance for STED experiments and advice on dye selection. Z.Z. contributed to STORM imaging. Q.L., C.L., and D.X. gave useful advice for designing the project. Q.P.S. and Y.S. supervised the project. M.Z., Q.P.S., and Y.S. wrote the manuscript.

DECLARATION OF INTERESTS

The authors declare no competing interests.

DECLARATION OF GENERATIVE AI AND AI-ASSISTED TECHNOLOGIES IN THE WRITING PROCESS

During the preparation of this work, the authors used ChatGPT (OpenAI) to assist with English language polishing. After using this tool, the authors carefully reviewed and edited the content and take full responsibility for the integrity and accuracy of the manuscript.

STAR★METHODS

Detailed methods are provided in the online version of this paper and include the following:

- KEY RESOURCES TABLE
- EXPERIMENTAL MODEL AND STUDY PARTICIPANT DETAILS
- METHOD DETAILS
  - Cell culture
  - Cell synchronization
  - DDK inhibition and SiRNA knockdown of PCNA
  - PCNA or lamin A/C overexpression
  - Click chemistry and immunofluorescence
  - DNA fiber assay
  - Flow cytometry analysis
  - BrdU-seq
  - Hi-C
  - ATAC-seq
  - Cut&Tag
  - RNA-seq
  - Stable cell line construction
  - Single-molecule tracking (SMT) and data analysis of PCNA
  - Chromatin loci dynamic tracking
  - Confocal and STED microscopy imaging and data analysis

- Expansion Microscopy (ExM) imaging and data analysis
- STORM imaging and data analysis
- QUANTIFICATION AND STATISTICAL ANALYSIS

SUPPLEMENTAL INFORMATION

Supplemental information can be found online at https://doi.org/10.1016/j.celrep.2026.117075.

Received: July 29, 2025
Revised: January 10, 2026
Accepted: February 11, 2026

REFERENCES

1. Rivera-Mulia, J.C., and Gilbert, D.M. (2016). Replicating large genomes: divide and conquer. Mol. Cell *62*, 756–765. https://doi.org/10.1016/j.molcel.2016.05.007.
2. Macheret, M., and Halazonetis, T.D. (2015). DNA replication stress as a hallmark of cancer. Annu. Rev. Pathol. *10*, 425–448. https://doi.org/10.1146/annurev-pathol-012414-040424.
3. Ganier, O., Prorok, P., Akerman, I., and Méchali, M. (2019). Metazoan DNA replication origins. Curr. Opin. Cell Biol. *58*, 134–141. https://doi.org/10.1016/j.ceb.2019.03.003.
4. Huberman, J.A., and Riggs, A.D. (1968). On the mechanism of DNA replication in mammalian chromosomes. J. Mol. Biol. *32*, 327–341. https://doi.org/10.1016/0022-2836(68)90013-2.
5. Lebofsky, R., Heilig, R., Sonnleitner, M., Weissenbach, J., and Bensimon, A. (2006). DNA replication origin interference increases the spacing between initiation events in human cells. Mol. Biol. Cell *17*, 5337–5345. https://doi.org/10.1091/mbc.E06-04-0298.
6. Hu, Y., and Stillman, B. (2023). Origins of DNA replication in eukaryotes. Mol. Cell *83*, 352–372. https://doi.org/10.1016/j.molcel.2022.12.024.
7. Hyrien, O. (2015). Peaks cloaked in the mist: the landscape of mammalian replication origins. J. Cell Biol. *208*, 147–160. https://doi.org/10.1083/jcb.201407004.
8. Lewis, J.S., Gross, M.H., Sousa, J., Henrikus, S.S., Greiwe, J.F., Nans, A., Diffley, J.F.X., and Costa, A. (2022). Mechanism of replication origin melting nucleated by CMG helicase assembly. Nature *606*, 1007–1014. https://doi.org/10.1038/s41586-022-04829-4.
9. Fragkos, M., Ganier, O., Coulombe, P., and Méchali, M. (2015). DNA replication origin activation in space and time. Nat. Rev. Mol. Cell Biol. *16*, 360–374. https://doi.org/10.1038/nrm4002.
10. Moldovan, G.-L., Pfander, B., and Jentsch, S. (2007). PCNA, the maestro of the replication fork. Cell *129*, 665–679. https://doi.org/10.1016/j.cell.2007.05.003.
11. Choe, K.N., and Moldovan, G.-L. (2017). Forging ahead through darkness: PCNA, still the principal conductor at the replication fork. Mol. Cell *65*, 380–392. https://doi.org/10.1016/j.molcel.2016.12.020.
12. Sogo, J.M., Lopes, M., and Foiani, M. (2002). Fork reversal and ssDNA accumulation at stalled replication forks owing to checkpoint defects. Science *297*, 599–602. https://doi.org/10.1126/science.1074023.
13. Jones, R.M., Mortusewicz, O., Afzal, I., Lorvellec, M., García, P., Helleday, T., and Petermann, E. (2013). Increased replication initiation and conflicts with transcription underlie Cyclin E-induced replication stress. Oncogene *32*, 3744–3753. https://doi.org/10.1038/onc.2012.387.
14. Böhly, N., Schmidt, A.-K., Zhang, X., Slusarenko, B.O., Hennecke, M., Kschischo, M., and Bastians, H. (2022). Increased replication origin firing links replication stress to whole chromosomal instability in human cancer. Cell Rep. *41*, 111836. https://doi.org/10.1016/j.celrep.2022.111836.
15. Fu, H., Redon, C.E., Thakur, B.L., Utani, K., Sebastian, R., Jang, S.-M., Gross, J.M., Mosavarpour, S., Marks, A.B., Zhuang, S.Z., et al. (2021). Dynamics of replication origin over-activation. Nat. Commun. *12*, 3448. https://doi.org/10.1038/s41467-021-23835-0.
16. Bester, A.C., Roniger, M., Oren, Y.S., Im, M.M., Sarni, D., Chaoat, M., Bensimon, A., Zamir, G., Shewach, D.S., and Kerem, B. (2011). Nucleotide deficiency promotes genomic instability in early stages of cancer development. Cell *145*, 435–446. https://doi.org/10.1016/j.cell.2011.03.044.
17. Marchal, C., Sima, J., and Gilbert, D.M. (2019). Control of DNA replication timing in the 3D genome. Nat. Rev. Mol. Cell Biol. *20*, 721–737. https://doi.org/10.1038/s41580-019-0162-y.
18. Nathanailidou, P., Taraviras, S., and Lygerou, Z. (2020). Chromatin and nuclear architecture: shaping DNA replication in 3D. Trends Genet. *36*, 967–980. https://doi.org/10.1016/j.tig.2020.07.003.
19. Chacin, E., Reusswig, K.-U., Furtmeier, J., Bansal, P., Karl, L.A., Pfander, B., Straub, T., Korber, P., and Kurat, C.F. (2023). Establishment and function of chromatin organization at replication origins. Nature *616*, 836–842. https://doi.org/10.1038/s41586-023-05926-8.
20. Jodkowska, K., Pancaldi, V., Rigau, M., Almeida, R., Fernández-Justel, J.M., Graña-Castro, O., Rodríguez-Acebes, S., Rubio-Camarillo, M., Carrillo-de Santa Pau, E., Pisano, D., et al. (2022). 3D chromatin connectivity underlies replication origin efficiency in mouse embryonic stem cells. Nucleic Acids Res. *50*, 12149–12165. https://doi.org/10.1093/nar/gkac1111.
21. Lee, C.S.K., Weiβ, M., and Hamperl, S. (2023). Where and when to start: regulating DNA replication origin activity in eukaryotic genomes. Nucleus *14*, 2229642. https://doi.org/10.1080/19491034.2023.2229642.
22. Kornberg, R.D. (1974). Chromatin structure: a repeating unit of histones and DNA. Science *184*, 868–871. https://doi.org/10.1126/science.184.4139.868.
23. Lieberman-Aiden, E., van Berkum, N.L., Williams, L., Imakaev, M., Ragoczy, T., Telling, A., Amit, I., Lajoie, B.R., Sabo, P.J., Dorschner, M.O., et al. (2009). Comprehensive mapping of long-range interactions reveals folding principles of the human genome. Science *326*, 289–293. https://doi.org/10.1126/science.1181369.
24. Dixon, J.R., Selvaraj, S., Yue, F., Kim, A., Li, Y., Shen, Y., Hu, M., Liu, J.S., and Ren, B. (2012). Topological domains in mammalian genomes identified by analysis of chromatin interactions. Nature *485*, 376–380. https://doi.org/10.1038/nature11082.
25. Misteli, T. (2020). The self-organizing genome: principles of genome architecture and function. Cell *183*, 28–45. https://doi.org/10.1016/j.cell.2020.09.014.
26. Ryba, T., Hiratani, I., Lu, J., Itoh, M., Kulik, M., Zhang, J., Schulz, T.C., Robins, A.J., Dalton, S., and Gilbert, D.M. (2010). Evolutionarily conserved replication timing profiles predict long-range chromatin interactions and distinguish closely related cell types. Genome Res. *20*, 761–770. https://doi.org/10.1101/gr.099655.109.
27. Dixon, J.R., Gorkin, D.U., and Ren, B. (2016). Chromatin domains: the unit of chromosome organization. Mol. Cell *62*, 668–680. https://doi.org/10.1016/j.molcel.2016.05.018.
28. Pope, B.D., Ryba, T., Dileep, V., Yue, F., Wu, W., Denas, O., Vera, D.L., Wang, Y., Hansen, R.S., Canfield, T.K., et al. (2014). Topologically associating domains are stable units of replication-timing regulation. Nature *515*, 402–405. https://doi.org/10.1038/nature13986.
29. Chagin, V.O., Casas-Delucchi, C.S., Reinhart, M., Schermelleh, L., Markaki, Y., Maiser, A., Bolius, J.J., Bensimon, A., Fillies, M., Domaing, P., et al. (2016). 4D Visualization of replication foci in mammalian cells corresponding to individual replicons. Nat. Commun. *7*, 11231. https://doi.org/10.1038/ncomms11231.
30. Sun, Y., Xu, X., Zhao, W., Zhang, Y., Chen, K., Li, Y., Wang, X., Zhang, M., Xue, B., Yu, W., et al. (2023). RAD21 is the core subunit of the cohesin complex involved in directing genome organization. Genome Biol. *24*, 155. https://doi.org/10.1186/s13059-023-02982-1.
31. Bintu, B., Mateo, L.J., Su, J.-H., Sinnott-Armstrong, N.A., Parker, M., Kinrot, S., Yamaya, K., Boettiger, A.N., and Zhuang, X. (2018). Super-resolution chromatin tracing reveals domains and cooperative interactions in

single cells. Science *362*, eaau1783. https://doi.org/10.1126/science.aau1783.

32. Su, Q.P., Zhao, Z.W., Meng, L., Ding, M., Zhang, W., Li, Y., Liu, M., Li, R., Gao, Y.Q., Xie, X.S., and Sun, Y. (2020). Superresolution imaging reveals spatiotemporal propagation of human replication foci mediated by CTCF-organized chromatin structures. Proc. Natl. Acad. Sci. USA *117*, 15036–15046. https://doi.org/10.1073/pnas.2001521117.
33. Li, Y., Xue, B., Zhang, M., Zhang, L., Hou, Y., Qin, Y., Long, H., Su, Q.P., Wang, Y., Guan, X., et al. (2021). Transcription-coupled structural dynamics of topologically associating domains regulate replication origin efficiency. Genome Biol. *22*, 206. https://doi.org/10.1186/s13059-021-02424-w.
34. Xiang, W., Roberti, M.J., Hériché, J.-K., Huet, S., Alexander, S., and Ellenberg, J. (2018). Correlative live and super-resolution imaging reveals the dynamic structure of replication domains. J. Cell Biol. *217*, 1973–1984. https://doi.org/10.1083/jcb.201709074.
35. Pownall, M.E., Miao, L., Vejnar, C.E., M'Saad, O., Sherrard, A., Frederick, M.A., Benitez, M.D.J., Boswell, C.W., Zaret, K.S., Bewersdorf, J., and Giraldez, A.J. (2023). Chromatin expansion microscopy reveals nanoscale organization of transcription and chromatin. Science *381*, 92–100. https://doi.org/10.1126/science.ade5308.
36. Faulkner, E.L., Pike, J.A., Densham, R.M., Garlick, E., Thomas, S.G., Neely, R.K., and Morris, J.R. (2022). Imaging nanoscale nuclear structures with expansion microscopy. J. Cell Sci. *135*, jcs259009. https://doi.org/10.1242/jcs.259009.
37. Shumaker, D.K., Kuczmarski, E.R., and Goldman, R.D. (2003). The nucleoskeleton: lamins and actin are major players in essential nuclear functions. Curr. Opin. Cell Biol. *15*, 358–366. https://doi.org/10.1016/S0955-0674(03)00050-4.
38. Hozák, P., Hassan, A.B., Jackson, D.A., and Cook, P.R. (1993). Visualization of replication factories attached to a nucleoskeleton. Cell *73*, 361–373. https://doi.org/10.1016/0092-8674(93)90235-i.
39. Lamm, N., Read, M.N., Nobis, M., Van Ly, D., Page, S.G., Masamsetti, V.P., Timpson, P., Biro, M., and Cesare, A.J. (2020). Nuclear F-actin counteracts nuclear deformation and promotes fork repair during replication stress. Nat. Cell Biol. *22*, 1460–1470. https://doi.org/10.1038/s41556-020-00605-6.
40. Parisis, N., Krasinska, L., Harker, B., Urbach, S., Rossignol, M., Camasses, A., Dewar, J., Morin, N., and Fisher, D. (2017). Initiation of DNA replication requires actin dynamics and formin activity. EMBO J. *36*, 3212–3231. https://doi.org/10.15252/embj.201796585.
41. Briand, N., and Collas, P. (2020). Lamina-associated domains: peripheral matters and internal affairs. Genome Biol. *21*, 85. https://doi.org/10.1186/s13059-020-02003-5.
42. Simon, D.N., and Wilson, K.L. (2011). The nucleoskeleton as a genome-associated dynamic 'network of networks'. Nat. Rev. Mol. Cell Biol. *12*, 695–708. https://doi.org/10.1038/nrm3207.
43. Adam, S.A. (2017). The nucleoskeleton. Cold Spring Harb. Perspect. Biol. *9*, a023556. https://doi.org/10.1101/cshperspect.a023556.
44. Haraguchi, T., Kojidani, T., Koujin, T., Shimi, T., Osakada, H., Mori, C., Yamamoto, A., and Hiraoka, Y. (2008). Live cell imaging and electron microscopy reveal dynamic processes of BAF-directed nuclear envelope assembly. J. Cell Sci. *121*, 2540–2554. https://doi.org/10.1242/jcs.033597.
45. Shimi, T., Kittisopikul, M., Tran, J., Goldman, A.E., Adam, S.A., Zheng, Y., Jaqaman, K., and Goldman, R.D. (2015). Structural organization of nuclear lamins A, C, B1, and B2 revealed by superresolution microscopy. Mol. Biol. Cell *26*, 4075–4086. https://doi.org/10.1091/mbc.E15-07-0461.
46. Dubik, N., and Mai, S. (2020). Lamin A/C: function in normal and tumor cells. Cancers *12*, 3688. https://doi.org/10.3390/cancers12123688.
47. Dittmer, T.A., and Misteli, T. (2011). The lamin protein family. Genome Biol. *12*, 222. https://doi.org/10.1186/gb-2011-12-5-222.
48. Nmezi, B., Xu, J., Fu, R., Armiger, T.J., Rodriguez-Bey, G., Powell, J.S., Ma, H., Sullivan, M., Tu, Y., Chen, N.Y., et al. (2019). Concentric organization of A-and B-type lamins predicts their distinct roles in the spatial organization and stability of the nuclear lamina. Proc. Natl. Acad. Sci. USA *116*, 4307–4315. https://doi.org/10.1073/pnas.1810070116.
49. Shimi, T., Pfleghaar, K., Kojima, S.-i., Pack, C.-G., Solovei, I., Goldman, A.E., Adam, S.A., Shumaker, D.K., Kinjo, M., Cremer, T., and Goldman, R.D. (2008). The A- and B-type nuclear lamin networks: microdomains involved in chromatin organization and transcription. Genes Dev. *22*, 3409–3421.
50. Bronshtein, I., Kepten, E., Kanter, I., Berezin, S., Lindner, M., Redwood, A.B., Mai, S., Gonzalo, S., Foisner, R., Shav-Tal, Y., and Garini, Y. (2015). Loss of lamin A function increases chromatin dynamics in the nuclear interior. Nat. Commun. *6*, 8044. https://doi.org/10.1038/ncomms9044.
51. De Vos, W.H., Houben, F., Hoebe, R.A., Hennekam, R., van Engelen, B., Manders, E.M.M., Ramaekers, F.C.S., Broers, J.L.V., and Van Oostveldt, P. (2010). Increased plasticity of the nuclear envelope and hypermobility of telomeres due to the loss of A–type lamins. Biochim. Biophys. Acta *1800*, 448–458. https://doi.org/10.1016/j.bbagen.2010.01.002.
52. Ranade, D., Pradhan, R., Jayakrishnan, M., Hegde, S., and Sengupta, K. (2019). Lamin A/C and Emerin depletion impacts chromatin organization and dynamics in the interphase nucleus. BMC Mol. Cell Biol. *20*, 11–20. https://doi.org/10.1186/s12860-019-0192-5.
53. Zheng, X., Hu, J., Yue, S., Kristiani, L., Kim, M., Sauria, M., Taylor, J., Kim, Y., and Zheng, Y. (2018). Lamins organize the global three-dimensional genome from the nuclear periphery. Mol. Cell *71*, 802–815.e7. https://doi.org/10.1016/j.molcel.2018.05.017.
54. Graziano, S., Kreienkamp, R., Coll-Bonfill, N., and Gonzalo, S. (2018). Causes and consequences of genomic instability in laminopathies: replication stress and interferon response. Nucleus *9*, 289–306. https://doi.org/10.1080/19491034.2018.1454168.
55. Willaume, S., Rass, E., Fontanilla-Ramirez, P., Moussa, A., Wanschoor, P., and Bertrand, P. (2021). A link between replicative stress, lamin proteins, and inflammation. Genes *12*, 552. https://doi.org/10.3390/genes12040552.
56. Capo-Chichi, C.D., Aguida, B., Chabi, N.W., Cai, Q.K., Offrin, G., Agossou, V.K., Sanni, A., and Xu, X.-X. (2016). Lamin A/C deficiency is an independent risk factor for cervical cancer. Cell. Oncol. *39*, 59–68. https://doi.org/10.1007/s13402-015-0252-6.
57. Cobb, A.M., Murray, T.V., Warren, D.T., Liu, Y., and Shanahan, C.M. (2016). Disruption of PCNA-lamins A/C interactions by prelamin A induces DNA replication fork stalling. Nucleus *7*, 498–511. https://doi.org/10.1080/19491034.2016.1239685.
58. Shumaker, D.K., Solimando, L., Sengupta, K., Shimi, T., Adam, S.A., Grunwald, A., Strelkov, S.V., Aebi, U., Cardoso, M.C., and Goldman, R.D. (2008). The highly conserved nuclear lamin Ig-fold binds to PCNA: its role in DNA replication. J. Cell Biol. *181*, 269–280. https://doi.org/10.1083/jcb.200708155.
59. Jackson, D.A., and Pombo, A. (1998). Replicon clusters are stable units of chromosome structure: evidence that nuclear organization contributes to the efficient activation and propagation of S phase in human cells. J. Cell Biol. *140*, 1285–1295. https://doi.org/10.1083/jcb.140.6.1285.
60. Ge, X.Q., Jackson, D.A., and Blow, J.J. (2007). Dormant origins licensed by excess Mcm2–7 are required for human cells to survive replicative stress. Genes Dev. *21*, 3331–3341. https://doi.org/10.1101/gad.457807.
61. Darzynkiewicz, Z., Halicka, H.D., Zhao, H., and Podhorecka, M. (2011). Cell synchronization by inhibitors of DNA replication induces replication stress and DNA damage response: analysis by flow cytometry. Methods Mol. Biol. *761*, 85–96. https://doi.org/10.1007/978-1-61779-182-6_6.
62. Johnson, B.R., Nitta, R.T., Frock, R.L., Mounkes, L., Barbie, D.A., Stewart, C.L., Harlow, E., and Kennedy, B.K. (2004). A-type lamins regulate retinoblastoma protein function by promoting subnuclear localization and preventing proteasomal degradation. Proc. Natl. Acad. Sci. USA *101*, 9677–9682. https://doi.org/10.1073/pnas.0403250101.

63. Graziano, S., Coll-Bonfill, N., Teodoro-Castro, B., Kuppa, S., Jackson, J., Shashkova, E., Mahajan, U., Vindigni, A., Antony, E., and Gonzalo, S. (2021). Lamin A/C recruits ssDNA protective proteins RPA and RAD51 to stalled replication forks to maintain fork stability. J. Biol. Chem. *297*, 101301. https://doi.org/10.1016/j.jbc.2021.101301.

64. Singh, M., Hunt, C.R., Pandita, R.K., Kumar, R., Yang, C.-R., Horikoshi, N., Bachoo, R., Serag, S., Story, M.D., Shay, J.W., et al. (2013). Lamin A/C depletion enhances DNA damage-induced stalled replication fork arrest. Mol. Cell Biol. *33*, 1210–1222. https://doi.org/10.1128/MCB.01676-12.

65. Hayashi, M.T., and Masukata, H. (2011). Regulation of DNA replication by chromatin structures: accessibility and recruitment. Chromosoma *120*, 39–46. https://doi.org/10.1007/s00412-010-0287-4.

66. Chanou, A., Weiβ, M., Holler, K., Sajid, A., Straub, T., Krietsch, J., Sanchi, A., Ummethum, H., Lee, C.S.K., Kruse, E., et al. (2023). Single molecule MATAC-seq reveals key determinants of DNA replication origin efficiency. Nucleic Acids Res. *51*, 12303–12324. https://doi.org/10.1093/nar/gkad1022.

67. Barth, R., Bystricky, K., and Shaban, H.A. (2020). Coupling chromatin structure and dynamics by live super-resolution imaging. Sci. Adv. *6*, eaaz2196. https://doi.org/10.1126/sciadv.aaz2196.

68. Ashwin, S.S., Nozaki, T., Maeshima, K., and Sasai, M. (2019). Organization of fast and slow chromatin revealed by single-nucleosome dynamics. Proc. Natl. Acad. Sci. USA *116*, 19939–19944. https://doi.org/10.1073/pnas.1907342116.

69. Oughtred, R., Rust, J., Chang, C., Breitkreutz, B.-J., Stark, C., Willems, A., Boucher, L., Leung, G., Kolas, N., Zhang, F., et al. (2021). The BioGRID database: A comprehensive biomedical resource of curated protein, genetic, and chemical interactions. Protein Sci. *30*, 187–200. https://doi.org/10.1002/pro.3978.

70. Kaya-Okur, H.S., Wu, S.J., Codomo, C.A., Pledger, E.S., Bryson, T.D., Henikoff, J.G., Ahmad, K., and Henikoff, S. (2019). CUT&Tag for efficient epigenomic profiling of small samples and single cells. Nat. Commun. *10*, 1930. https://doi.org/10.1038/s41467-019-09982-5.

71. Naetar, N., Korbei, B., Kozlov, S., Kerenyi, M.A., Dorner, D., Kral, R., Gotic, I., Fuchs, P., Cohen, T.V., Bittner, R., et al. (2008). Loss of nucleoplasmic LAP2alpha-lamin A complexes causes erythroid and epidermal progenitor hyperproliferation. Nat. Cell Biol. *10*, 1341–1348. https://doi.org/10.1038/ncb1793.

72. Dorner, D., Vlcek, S., Foeger, N., Gajewski, A., Makolm, C., Gotzmann, J., Hutchison, C.J., and Foisner, R. (2006). Lamina-associated polypeptide 2α regulates cell cycle progression and differentiation via the retinoblastoma–E2F pathway. J. Cell Biol. *173*, 83–93. https://doi.org/10.1083/jcb.200511149.

73. Los, G.V., Encell, L.P., McDougall, M.G., Hartzell, D.D., Karassina, N., Zimprich, C., Wood, M.G., Learish, R., Ohana, R.F., Urh, M., et al. (2008). HaloTag: a novel protein labeling technology for cell imaging and protein analysis. ACS Chem. Biol. *3*, 373–382. https://doi.org/10.1021/cb800025k.

74. Moiseeva, T., Hood, B., Schamus, S., O'Connor, M.J., Conrads, T.P., and Bakkenist, C.J. (2017). ATR kinase inhibition induces unscheduled origin firing through a Cdc7-dependent association between GINS and And-1. Nat. Commun. *8*, 1392. https://doi.org/10.1038/s41467-017-01401-x.

75. Moiseeva, T.N., Yin, Y., Calderon, M.J., Qian, C., Schamus-Haynes, S., Sugitani, N., Osmanbeyoglu, H.U., Rothenberg, E., Watkins, S.C., and Bakkenist, C.J. (2019). An ATR and CHK1 kinase signaling mechanism that limits origin firing during unperturbed DNA replication. Proc. Natl. Acad. Sci. USA *116*, 13374–13383. https://doi.org/10.1073/pnas.1903418116.

76. Wang, Y., Elsherbiny, A., Kessler, L., Cordero, J., Shi, H., Serke, H., Lityagina, O., Trogisch, F.A., Mohammadi, M.M., El-Battrawy, I., et al. (2022). Lamin A/C-dependent chromatin architecture safeguards naïve pluripotency to prevent aberrant cardiovascular cell fate and function. Nat. Commun. *13*, 6663. https://doi.org/10.1038/s41467-022-34366-7.

77. Köhler, C., Koalick, D., Fabricius, A., Parplys, A.C., Borgmann, K., Pospiech, H., and Grosse, F. (2016). Cdc45 is limiting for replication initiation in humans. Cell Cycle *15*, 974–985. https://doi.org/10.1080/15384101.2016.1152424.

78. Johnson, C., Gali, V.K., Takahashi, T.S., and Kubota, T. (2016). PCNA retention on DNA into G2/M phase causes genome instability in cells lacking Elg1. Cell Rep. *16*, 684–695. https://doi.org/10.1016/j.celrep.2016.06.030.

79. Fukami-Kobayashi, J., and Mitsui, Y. (1999). Overexpression of proliferating cell nuclear antigen in mammalian cells negates growth arrest by serum starvation and cell contact. Jap. J. Cancer Res. *90*, 286–293. https://doi.org/10.1111/j.1349-7006.1999.tb00746.x.

80. Baris, Y., Taylor, M.R.G., Aria, V., and Yeeles, J.T.P. (2022). Fast and efficient DNA replication with purified human proteins. Nature *606*, 204–210. https://doi.org/10.1038/s41586-022-04759-1.

81. Arbel, M., Choudhary, K., Tfilin, O., and Kupiec, M. (2021). PCNA loaders and unloaders—One ring that rules them all. Genes *12*, 1812. https://doi.org/10.3390/genes12111812.

82. Langmead, B., and Salzberg, S.L. (2012). Fast gapped-read alignment with Bowtie 2. Nat. Methods *9*, 357–359. https://doi.org/10.1038/nmeth.1923.

83. Zhang, Y., Liu, T., Meyer, C.A., Eeckhoute, J., Johnson, D.S., Bernstein, B.E., Nusbaum, C., Myers, R.M., Brown, M., Li, W., and Liu, X.S. (2008). Model-based analysis of ChIP-Seq (MACS). Genome Biol. *9*, R137. https://doi.org/10.1186/gb-2008-9-9-r137.

84. Servant, N., Varoquaux, N., Lajoie, B.R., Viara, E., Chen, C.-J., Vert, J.-P., Heard, E., Dekker, J., and Barillot, E. (2015). HiC-Pro: an optimized and flexible pipeline for Hi-C data processing. Genome Biol. *16*, 259. https://doi.org/10.1186/s13059-015-0831-x.

85. Schindelin, J., Arganda-Carreras, I., Frise, E., Kaynig, V., Longair, M., Pietzsch, T., Preibisch, S., Rueden, C., Saalfeld, S., Schmid, B., Tinevez, J.-Y., White, D.J., Hartenstein, V., Eliceiri, K., Tomancak, P., and Cardona, A. (2012). Fiji: an open-source platform for biological-image analysis. Nat. Methods *9*, 676–682. https://doi.org/10.1038/nmeth.2019.

86. Tinevez, J.-Y., Perry, N., Schindelin, J., Hoopes, G.M., Reynolds, G.D., Laplantine, E., Bednarek, S.Y., Shorte, S.L., and Eliceiri, K.W. (2017). TrackMate: an open and extensible platform for single-particle tracking. Methods *115*, 80–90. https://doi.org/10.1016/j.ymeth.2016.09.016.

87. Ovesný, M., Křížek, P., Borkovec, J., Švindrych, Z., and Hagen, G.M. (2014). ThunderSTORM: a comprehensive ImageJ plug-in for PALM and STORM data analysis and super-resolution imaging. Bioinformatics *30*, 2389–2390. https://doi.org/10.1093/bioinformatics/btu202.

88. Levet, F., Hosy, E., Kechkar, A., Butler, C., Beghin, A., Choquet, D., and Sibarita, J.-B. (2015). SR-Tesseler: a method to segment and quantify localization-based super-resolution microscopy data. Nat. Methods *12*, 1065–1071. https://doi.org/10.1038/nmeth.3579.

89. Marchal, C., Sasaki, T., Vera, D., Wilson, K., Sima, J., Rivera-Mulia, J.C., Trevilla-García, C., Nogues, C., Nafie, E., and Gilbert, D.M. (2018). Genome-wide analysis of replication timing by next-generation sequencing with E/L Repli-seq. Nat. Protoc. *13*, 819–839. https://doi.org/10.1038/nprot.2017.148.

90. Love, M.I., Huber, W., and Anders, S. (2014). Moderated estimation of fold change and dispersion for RNA-seq data with DESeq2. Genome Biol. *15*, 550. https://doi.org/10.1186/s13059-014-0550-8.

91. Guilbaud, G., Rappailles, A., Baker, A., Chen, C.-L., Arneodo, A., Goldar, A., d'Aubenton-Carafa, Y., Thermes, C., Audit, B., and Hyrien, O. (2011). Evidence for sequential and increasing activation of replication origins along replication timing gradients in the human genome. PLoS Comput. Biol. *7*, e1002322. https://doi.org/10.1371/journal.pcbi.1002322.

92. Conti, C., Saccà, B., Herrick, J., Lalou, C., Pommier, Y., and Bensimon, A. (2007). Replication fork velocities at adjacent replication origins are

coordinately modified during DNA replication in human cells. Mol. Biol. Cell *18*, 3059–3067. https://doi.org/10.1091/mbc.e06-08-0689.

93. Imakaev, M., Fudenberg, G., McCord, R.P., Naumova, N., Goloborodko, A., Lajoie, B.R., Dekker, J., and Mirny, L.A. (2012). Iterative correction of Hi-C data reveals hallmarks of chromosome organization. Nat. Methods *9*, 999–1003. https://doi.org/10.1038/nmeth.2148.

94. Buenrostro, J.D., Giresi, P.G., Zaba, L.C., Chang, H.Y., and Greenleaf, W.J. (2013). Transposition of native chromatin for fast and sensitive epigenomic profiling of open chromatin, DNA-binding proteins and nucleosome position. Nat. Methods *10*, 1213–1218. https://doi.org/10.1038/nmeth.2688.

95. Quinlan, A.R., and Hall, I.M. (2010). BEDTools: a flexible suite of utilities for comparing genomic features. Bioinformatics *26*, 841–842. https://doi.org/10.1093/bioinformatics/btq033.

96. Dobin, A., Davis, C.A., Schlesinger, F., Drenkow, J., Zaleski, C., Jha, S., Batut, P., Chaisson, M., and Gingeras, T.R. (2013). STAR: ultrafast universal RNA-seq aligner. Bioinformatics *29*, 15–21. https://doi.org/10.1093/bioinformatics/bts635.

97. Chang, L., Li, M., Shao, S., Li, C., Ai, S., Xue, B., Hou, Y., Zhang, Y., Li, R., Fan, X., et al. (2022). Nuclear peripheral chromatin-lamin B1 interaction is required for global integrity of chromatin architecture and dynamics in human cells. Protein Cell *13*, 258–280. https://doi.org/10.1007/s13238-020-00794-8.

98. Shao, S., Zhang, H., Zeng, Y., Li, Y., Sun, C., and Sun, Y. (2021). TagBiFC technique allows long-term single-molecule tracking of protein-protein interactions in living cells. Commun. Biol. *4*, 378. https://doi.org/10.1038/s42003-021-01896-7.

STAR★METHODS

KEY RESOURCES TABLE

REAGENT or RESOURCE	SOURCE	IDENTIFIER
Antibodies		
Mouse anti-BrdU (B44)	BD Biosciences	Cat# 555627; RRID: AB_395993
Rabbit anti-PCNA	Cell Signaling Technology	Cat# 13110; RRID: AB_2636979
Rabbit anti-Lamin A/C	Cell Signaling Technology	Cat# 4777; RRID: AB_10545756
Rabbit anti-pH2AX	Cell Signaling Technology	Cat# 9718; RRID: AB_2118009
Rabbit anti-CTCF	Abcam	Cat# ab128873; RRID: AB_11144295
Rabbit anti-pRPA (S33)	Abcam	Cat# ab211877; RRID: AB_2818947
Secondary antibodies (various conjugates: Alexa Fluor, STAR Red, STAR Orange, etc.)	Thermo Fisher, Abberior, etc.	see method details
Chemicals, peptides, and recombinant proteins		
Dulbecco's Modified Eagle Medium (DMEM)	Gibco	Cat# 11965-092
Penicillin-Streptomycin	Gibco	Cat# 15140-122
Trypsin (0.25%)	Gibco	Cat# 25200-056
Thymidine	Sigma-Aldrich	Cat# T1895
Aphidicolin	Sigma-Aldrich	Cat# A0781
BrdU	Sigma-Aldrich	Cat# B5002
EdU	Thermo Fisher Scientific	Cat# C10337
Bovine Serum Albumin (BSA)	Sigma-Aldrich	Cat# A7906
Triton X-100	Sigma-Aldrich	Cat# T8787
SIR azide	CONFLUORE	Cat# BSR-2-1mg
RIPA buffer	Yeasen	Cat# 20101ES60
Vazyme magnetic beads	Vazyme	Cat# N401-01
Protein G-Dynabeads	Invitrogen	Cat# 10004D
Formaldehyde (PFA)	Sigma-Aldrich	Cat# F8775
Acrylamide (AaM)	Sigma-Aldrich	Cat# A9099
Sodium acrylate (SA)	Sigma-Aldrich	Cat# 408220
N,N′-methylenebisacrylamide (DHEBA)	Sigma-Aldrich	Cat# 146072
TEMED	Sigma-Aldrich	Cat# T9281
Ammonium persulfate (APS)	Sigma-Aldrich	Cat# A3678
Nocodazole	Sigma-Aldrich	Cat# M1404
XL413	MCE	Cat# HY-15260
GP-transfect-Mate	GenePharma	Cat# G04008
Neofect transfection reagent	Neofect	Cat# TF201201
Critical commercial assays		
Click-iT EdU Imaging Kit	Thermo Fisher Scientific	Cat# C10337
Vazyme CUT&Tag kit	Vazyme	Cat# TD904
Vazyme library prep kits	Vazyme	Cat# NE103, Cat# TD202/TD203
Deposited data		
Raw and processed sequencing data (BrdU-seq, Hi-C, ATAC-seq, RNA-seq, Cut&Tag)	GEO	GEO: GSE289473, GSE289474, GSE289475
Experimental models: cell lines		
HeLa S3	Kind gift from Dr. Wei Guo, University of Pennsylvania	N/A

(*Continued on next page*)

Continued

REAGENT or RESOURCE	SOURCE	IDENTIFIER
MD-MBA-231	Kind gift from Dr. Wei Guo, University of Pennsylvania	N/A
Lamin A/C knockout–HeLa S3	This study	N/A
Lamin A/C knockout–MDA-MB-231	This study	N/A
Halotag-PCNA-HeLa S3	This study	N/A
Oligonucleotides		
PCNA-targeting siRNA	GenePharma	GACCAGGCGCGCCTCGAACA
sgRNA for Lamin A/C knockouts	Tsingke	HeLa S3: 5′-CGTCATGAGACCCGACTGG-3’; MDA-MB-231: 5′-CGTCATGAGACCCGACTGG-3′ and 5′-CATCGACCGTGTGCGCTCGC-3
Recombinant DNA		
lentiCRISPR v2	Addgene	52961
psPAX2	Addgene	12260
pMD2.G	Addgene	12259
Cas9-sgRNA plasmid (PX330)	Addgene	42230
HaloTag-PCNA donor plasmid	Addgene	170818
Software and algorithms		
Bowtie2	Langmead and Salzberg[82]	http://bowtie-bio.sourceforge.net/bowtie2
MACS2	Zhang et al.[83]	https://github.com/macs3-project/MACS
DiffBind	R Bioconductor	https://bioconductor.org/packages/release/bioc/html/DiffBind.html
DESeq2	R Bioconductor	https://bioconductor.org/packages/release/bioc/html/DESeq2.html
ChIPseeker	R Bioconductor	https://bioconductor.org/packages/release/bioc/html/ChIPseeker.html
IGV	Broad Institute	https://software.broadinstitute.org/software/igv/
HiC-Pro	Servant et al.[84]	https://github.com/nservant/HiC-Pro
Huygens Professional	Scientific Volume Imaging	https://svi.nl/Huygens-Professional
Fiji	Schindelin et al.[85]	https://fiji.sc/
TrackMate	Tinevez et al.[86]	https://imagej.net/plugins/trackmate/
ThunderSTORM	Ovesný et al.[87]	https://zitmen.github.io/thunderstorm/
SR-Tesseler	Levet et al.[88]	http://nautica.u-strasbg.fr/srtesseler/
Custom MATLAB scripts	This study	NA
Custom Python scripts	This study	NA
GraphPad Prism	GraphPad	version 9
Other		
35 mm glass-bottom dish	Cellvis	Cat# D35-20-1.5-N
TetraSpeck Microspheres	Thermo Fisher Scientific	Cat# T7279
Nikon N-STORM microscope	Nikon	Ni-E
Abberior STED microscope	Abberior	Stedycon
Olympus IX83 microscope	Olympus	IX83
Andor EMCCD camera	Andor	Ixon Ultra EMCCD

EXPERIMENTAL MODEL AND STUDY PARTICIPANT DETAILS

This study utilized HeLa S3 and MDA-MB-231 cell lines. Lamin A/C KO cell lines were generated from both HeLa S3 and MDA-MB-231 cells. A HeLa S3 cell line stably expressing PCNA-HaloTag was also established. All cell lines were cultured and generated as described in the method details section below.

METHOD DETAILS

Cell culture

HeLa S3 cells and MDA-MB-231 cells were cultured in 10 cm plastic dishes (Corning, 430167) or 35 mm glass-bottom dishes (Cellvis, D35-20-1.5-N) to facilitate monitoring and imaging. The cells were maintained in Dulbecco's Modified Eagle Medium (DMEM, Gibco, 11965-092) supplemented with 10% fetal bovine serum (Gibco, 10099-141) and 100 U/mL penicillin-streptomycin (Gibco, 15140-122). Cultures were incubated at 37°C in a humidified atmosphere containing 5% CO_2 (Thermo Scientific, Forma Series II). Cell lines were authenticated by short tandem repeat (STR) profiling following ANSI/ATCC ASN-0002-2011 guidelines. Cells were routinely tested for mycoplasma contamination and were negative throughout the study. Cell growth was monitored regularly, and subculturing was performed every 2–3 days when confluency reached approximately 80%, using 0.25% trypsin (Gibco, 25200-056).

Cell synchronization

To synchronize the cell cycle at the G1/S transition, a combination of thymidine and aphidicolin was employed (Figure S2A). Cells were treated with 2 mM thymidine (Sigma-Aldrich, T1895) for 16 h to block DNA synthesis. Following three washes with PBS (Gibco, C14190500BT), cells were incubated in fresh DMEM for 10 h. Aphidicolin (Sigma-Aldrich, A0781) was then added at a final concentration of 2 μg/mL for 16 h, effectively enhancing the synchronization at the G1/S transition. The following release was conducted using 10 μM EdU or 16 μM BrdU in DMEM, with varying incubation duration, as described respectively in the article.

In the non-aphidicolin-induced approach (Figure S8A), cells were synchronized in the M phase using nocodazole (Sigma-Aldrich, M1404), which inhibits spindle formation. Cells were incubated with 100 ng/μL nocodazole for 16 h. Detached mitotic cells were collected by gently shaking the culture dishes, and after centrifugation, the cells were washed three times with PBS. The cells were subsequently released into DMEM containing 10 μM EdU (Thermo Fisher Scientific, C10337) for 8 h to label cells entering early S phase.

DDK inhibition and SiRNA knockdown of PCNA

Where indicated, CDC7/DBF4 (DDK) activity was inhibited using the small-molecule DDK inhibitor XL413 (MCE, HY-15260). Cells were synchronized at the G1/S transition as described above. One hour before release into S phase, cells were pre-incubated with XL413 (10 μM) in fresh pre-warmed DMEM. At the time of release, the medium was replaced with fresh pre-warmed medium containing 10 μM EdU (10 min pulse for replication labeling), while maintaining XL413 at 10 μM. Cells were then fixed and processed as described in the corresponding sections.

For partial depletion of PCNA, Lamin A/C-deficient HeLa cells were transfected with small interfering RNAs targeting PCNA (sense 5′-GCGUGAACCUCACCAGUAUTT-3′, antisense 5′-AUACUGGUGAGGUUCACGCTT-3′) using GP-transfect-Mate (GenePharma, G04008) according to the manufacturer's instructions. siRNAs were transfected at a final concentration of 75 nM in Opti-MEM 6 h before thymidine treatment for synchronization to the G1/S transition. Cells were then released, fixed, and labeled as described in the corresponding sections.

PCNA or lamin A/C overexpression

Transient overexpression of PCNA or Lamin A/C was performed using mammalian expression plasmids encoding human PCNA-GFP or Lamin A/C-GFP (pcDNA3.1 backbone). HeLa cells were seeded onto glass-bottom dishes and transfected at ~20% confluency using Neofect (TF201201) following the manufacturer's protocol. Cells were transfected with 2 μg plasmid DNA per well and incubated for 6 h prior to thymidine treatment for synchronization to the G1/S transition. Cells were then released, fixed, and labeled as described in the corresponding sections.

Click chemistry and immunofluorescence

Click chemistry and immunofluorescence staining were used to detect DNA replication events and specific proteins. Cells were fixed and washed with PBS. To reduce non-specific binding, the samples were blocked in PBS containing 5% bovine serum albumin (BSA, Sigma-Aldrich, A7906) and 0.5% Triton X-100 (Sigma-Aldrich, T8787) for 45 min.

For click chemistry, the Click-iT EdU Imaging Kit (Thermo Fisher Scientific, C10337) was used to label EdU with the included AF647 dye for STORM experiments or with 10 μM SIR dye for other experiments. When SIR dye was used for clicking, DMSO was added at a final concentration of 10% to enhance dye isolation.

For immunofluorescence, Primary antibodies against BrdU (BD, B44), PCNA (CST, 13110), Lamin A/C (CST, 4777), pH2AX (CST, 9718), pRPA-S33 (ab211877), and CTCF (Abcam, ab128873) were diluted 1:200 in PBS with 5% BSA and 0.5% Triton X-100. For PCNA labeling, pre-treatment with cold methanol at −20°C was performed for 10 min prior to primary antibody incubation, following the manufacturer's instructions. The samples were incubated with primary antibodies at room temperature for 1 h, followed by four washes with PBS containing 1% Triton X-100. Secondary antibodies conjugated to different dyes, chosen to suit specific imaging experiments (STED, ExM, and STORM), were applied at a 1:50 dilution and incubated for 1 h. After another series of washes, the samples were stored in PBS at 4°C, protected from light until imaging.

DNA fiber assay

The DNA fiber assay was used to measure replication fork progression and inter-track distance in synchronized cells. For replication fork progression measurements, HeLa cells were synchronized at the G1/S transition and released into S phase by washing three times with PBS, followed by incubation in DMEM containing 40 μM CldU and then 100 μM IdU, each for 20 min. For inter-track distance measurements, cells were synchronized at the G1/S transition and released into early S phase in DMEM containing 40 μM CldU for 10 min, followed by 100 μM IdU for 50 min to label the replicated DNA backbone.

Cells were harvested using trypsin, resuspended in PBS, and collected by centrifugation. The cell pellet was washed three times in PBS, and 100 μL of lysis buffer (200 mM Tris-HCl (Sigma-Aldrich, T5941), 50 mM EDTA (Sigma-Aldrich, E6758), and 0.5% SDS (Sigma-Aldrich, L3771)) was added.

For DNA fiber, lysed DNA was applied to silanized coverslips and allowed to dry at room temperature for 3–5 min. Coverslips were tilted at an approximately 15-degree angle to allow the gradual flow of the buffer, ensuring uniform DNA stretching. After air drying, the DNA was fixed using a 3:1 methanol (Sigma-Aldrich, M1775)/acetic acid (Sigma-Aldrich, A6283) mixture. Newly synthesized DNA was labeled using immunofluorescence with anti-CldU (BD, B1/75) and anti-IdU (BD, B44) antibodies. For replication fork measurements, the lengths of individual CldU–IdU tracks were measured manually. Replication fork speed was calculated by converting physical fiber lengths into kilobases using a factor of 2 kb/μm. For inter-track distance, we measured the center-to-center distance between adjacent, clearly separated CldU-positive tracks along the same IdU-positive fiber; overlapping or ambiguous fibers were excluded from analysis.

Flow cytometry analysis

Flow cytometry was performed to quantify cell cycle progression. HeLa cells were incubated in 30 μM BrdU (Sigma-Aldrich, B5002) for 60 min, then washed with PBS and trypsinized. After resuspension in DMEM containing 10% fetal bovine serum (FBS; Sigma-Aldrich, F2442), cells were collected by centrifugation at 200*g* for 3 min. They were washed twice with PBS and fixed by adding ice-cold 70% ethanol in a 3:1 ratio with PBS, followed by storage at −20°C overnight.

The next day, cells were washed twice with PBS, resuspended in PBS, and treated with 100 μg/mL RNase A (Sigma-Aldrich, R6513) and 0.2% Triton X-100 (Sigma-Aldrich, X100) at 37°C for 30 min. Propidium iodide (PI; Solarbio, P8080-10) was added at a final concentration of 50 μg/mL, and the cells were incubated for 30 min at room temperature. Flow cytometry was conducted using a BD analyzer, with a minimum of 10,000 cells collected per sample. Debris and doublets were excluded by gating on FSC-A/SSC-A and PE-A/PE-W plots. Data were analyzed to determine the proportion of cells in the S phase, with voltage adjustments made to ensure accurate separation of G1, S, and G2/M phases in PI-A histograms.

BrdU-seq

BrdU-seq (5-bromo-2′-deoxyuridine sequencing) was modified from the previous study[89] for replication initiation detection. Cells were synchronized at the G1/S transition and labeled for 10 min to correspond with imaging results.

HeLa cells were cultured in 10 cm dishes at a density of ∼20%, then synchronized at either the G1/S transition or specific points in S phase. After synchronization, cells were washed three times with PBS. BrdU (Sigma-Aldrich, B5002) was added to the medium to label replicating DNA for specific durations. Following labeling, cells were washed with PBS and lysed in RIPA buffer (Yeasen, 20101ES60) containing RNase A (Qiagen, 19101) and Proteinase K (Thermo Fisher Scientific, EO0491) at final concentrations of 0.1 mg/mL and 0.2 mg/mL, respectively. Lysis was carried out in a thermomixer first at 37°C for 2 h, followed by 55°C for 5 h to ensure complete cell lysis and DNA release.

Genomic DNA was extracted from the lysate using phenol-chloroform extraction to ensure purity. DNA was mixed with phenol-chloroform-isoamyl alcohol (24:25:1) at a 1:1 ratio, shaken for 5 min, and allowed to settle for phase separation. After centrifugation (15,000 g, 10 min), the upper aqueous phase containing the DNA was collected. The extraction was repeated, and the DNA was precipitated with ethanol and 3 M sodium acetate (pH 5.5). DNA was pelleted by centrifugation (16,000 g, 30 min at 4°C), washed with 75% ethanol, air-dried, and resuspended in ultrapure water.

The extracted DNA was fragmented into ∼200 bp fragments using a Covaris sonicator (175 W, 10% duty cycle, 200 cycles per burst). Fragmented DNA was then purified using Vazyme magnetic beads (Vazyme, N401-01). Following DNA fragmentation, BrdU-labeled DNA was denatured to single-stranded DNA by heat treatment. The denatured DNA was incubated with BrdU-specific antibodies (BD, 555627) in an immunoprecipitation buffer. Protein G-Dynabeads (Invitrogen, 10004D) were used to capture the antibody-DNA complexes. The immunoprecipitated DNA was washed extensively, and the DNA was eluted with TE buffer. The recovered DNA fragments were used to generate sequencing libraries with the Vazyme single-strand DNA library preparation kit (Vazyme, NE103). Libraries were sequenced on an Illumina platform.

Sequencing data were preprocessed to remove low-quality reads, and adapter sequences were trimmed using Trim Galore. Processed reads were aligned to the human reference genome (hg19) using Bowtie2. Peak calling was performed using MACS2[83] to identify BrdU-enriched regions. Visualization of BrdU-labeled regions was done using the Integrative Genomics Viewer (IGV). Differential analysis between WT and Lamin A/C KO cell lines was conducted using DiffBind and DESeq2,[90] with significant peaks identified by thresholds of $p < 0.05$ and log2FoldChange >1 or < −1. When considering the reported fork speed (∼1 Kbp/min),[91,92] an estimated 10-min replication peak length of ∼10 Kbp was chosen to select the peak containing at least one early replication site.

Hi-C

Hi-C was performed as described previously.[23] HeLa cells were cross-linked with 3% formaldehyde at room temperature for 10 min, followed by quenching with 0.125 M glycine. Nuclei were isolated, and chromatin was digested using a restriction enzyme, HindIII, for 16 h at 37°C. Digested DNA ends were biotinylated and ligated *in situ* to create proximity ligation products. Cross-links were reversed, and the DNA was purified. Biotin-labeled ligation junctions were isolated using streptavidin-coated beads, and the libraries were prepared using standard Illumina sequencing protocols.

Sequencing reads were aligned to the reference genome hg19, and interaction maps were generated using the computational tools HiC-Pro.[84] Hi-C raw matrices were normalized by ICE (iterative correction and eigenvector decomposition).[93] After normalization, the genome-wide relative contact maps are comparable among each sample; the subsequent analysis was based on the normalized matrix. The genome was partitioned into A/B compartments according to the first principal component values: positive values defined compartment A (higher gene density), while negative values defined compartment B. For TAD analysis, we utilized ICE-normalized matrices at a 40-kb resolution to identify TADs using the Perl script matrix2insulation.pl (http://github.com/blajoie/crane-nature-2015).

ATAC-seq

ATAC-seq was performed to assess chromatin accessibility as previously described.[94] Briefly, nuclei were extracted from G1/S-transition synchronized cells using lysis buffer and centrifuged at 500×g for 5 min at 4°C. Nuclei pellets were resuspended in the Tn5 transposase reaction mix and incubated at 37°C for 30 min. Following transposition, equimolar adapters were ligated, and the resulting libraries were amplified by PCR. Libraries were purified using AMPure beads and quantified using a Qubit fluorometer. Sequencing was conducted on an Illumina NovaSeq 6000 platform with 150 bp paired-end reads.

Raw sequencing reads were processed to remove adapters, poly-N sequences, and low-quality reads (base quality <15 for >40% of reads). Clean reads were aligned to the reference genome hg19 using Bowtie2.[82] Reads derived from mitochondrial DNA or with low mapping quality (MAPQ <13) were excluded. Only uniquely mapped and de-duplicated reads were retained for analysis. Peak calling was performed using MACS2 (v2.2.7.1) with the default parameters. Identified peaks were annotated using ChIPseeker to associate them with nearby genes, followed by Gene Ontology (GO) and KEGG pathway enrichment analyses to identify functional enrichment. Differential peak analysis between groups was performed using Bedtools,[95] with differential peaks defined as having a fold change >2 ($|\log2FC| > 1$). All experiments were conducted in triplicate to ensure reproducibility, and statistical significance was determined with a threshold of $p < 0.05$.

Cut&Tag

The Cut&Tag protocol was adapted from a previous study[70] for efficient profiling of chromatin-bound factors. Cut&Tag was performed using the Vazyme CUT&Tag kit (#TD904) according to the manufacturer's instructions, with minor modifications. Briefly, approximately 100,000 HeLa cells were harvested and permeabilized with digitonin in wash buffer. ConA beads were activated and incubated with cells at room temperature for 10 min. Primary antibodies(PCNA) against the target protein were added, and the reaction was incubated overnight at 4°C. The next day, samples were washed and incubated with a secondary antibody conjugated to Protein A-Tn5 transposase. Following tagmentation, DNA was extracted using DNA Clean Beads (Vazyme #N411) and purified. The libraries were amplified using the Vazyme library amplification primers (#TD202/TD203) and sequenced on an Illumina NovaSeq 6000 platform. Sequencing reads were aligned to the reference genome, and peaks were called using MACS2.[83] The subsequent analysis process was the same as that of ATAC-seq.

RNA-seq

Total RNA was extracted and its integrity assessed using the RNA Nano 6000 Assay Kit on the Bioanalyzer 2100 system (Agilent Technologies). mRNA was enriched using poly-T magnetic beads, fragmented, and reverse transcribed into cDNA. Following end repair, A-tailing, and adaptor ligation, 370–420 bp cDNA fragments were selected, PCR amplified, and subjected to quality control using a Qubit Fluorometer, Agilent 2100, and qRT-PCR to ensure effective library concentrations (>2 nM). Qualified libraries were sequenced on the Illumina NovaSeq 6000 platform, generating 150 bp paired-end reads. Raw data were processed to remove low-quality reads and adapters, producing high-quality clean reads. Reads were mapped to the reference genome using STAR,[96] and gene expression levels were quantified as FPKM using featureCounts, accounting for sequencing depth and gene length. Differential expression analysis was performed using the DESeq2[90] R package (v1.20.0) with two biological replicates per condition. Significant genes were identified based on padj <0.05 and $|\log2(\text{fold change})| > 1$. Genes with p-value <0.05 and fold change >0.5 were further analyzed in DAVID (KEGG and GO analysis were focused). Terms with FDR <0.05 were ranked by count, and the top 10 pathways with the highest counts were selected for display.

Stable cell line construction

Lamin A/C KO cell line: sgRNAs targeting Lamin A/C (CGTCATGAGACCCGACTGG for HeLa S3, CGTCATGAGACCCGACTGG and CATCGACCGTGTGCGCTCGC for MDA-MB-231) were respectively inserted into the lentiCRISPR v2 vector. Lentiviral particles were generated by co-transfecting HEK293T cells with lentiCRISPR v2, psPAX2, and pMD2.G plasmids in a 5:3:2 ratio using PEI MAX 40000 (Polysciences, USA). The viral supernatants were harvested 48 h after transfection and concentrated by ultracentrifugation

at 20,000 × g for 90 min at 4°C. MDA-MB-231 cells were infected with the concentrated lentivirus in the presence of 8 μg/mL polybrene (Sigma-Aldrich, USA). Transduced cells underwent selection with 2 μg/mL puromycin 48 h post-infection. Individual clones were isolated using flow cytometry, and the KO of Lamin A/C was verified through Western blotting.

PCNA-HaloTag cell line: To study PCNA dynamics, a stable HeLa cell line expressing PCNA-HaloTag was constructed. The sgRNA sequence, GACCAGGCGCGCCTCGAACA, was used to introduce a HaloTag at the PCNA locus via homology-directed repair. HeLa cells were co-transfected with Cas9-sgRNA plasmids (adapted from Addgene-42230) and a donor plasmid containing the HaloTag-PCNA homology arms (adapted from Addgene-170818). Following transfection, cells were labeled with JF594 HaloTag ligand and sorted using flow cytometry. Successful integration was confirmed by PCR and immunoblotting.

sfGFP Cell line for chromatin loci tracking: The construction was performed using plasmids and protocols identical to those described in our lab's previous work.[97] Briefly, WT and Lamin A/C KO HeLa cells were seeded into 6-well plates at approximately 50% confluency one day prior to transfection. Each well was transfected with pB-TRE3G-NLSSV40-dCas9-3X NLSSV40-24X GCN4-V4-NLSSV40-P2A-BFP-PuroR-P2A-rtTA plasmid, pB-TRE3G-ScFV-sfGFP-GB1-NLSSV40-HygroR-P2A-rtTA plasmid, and pCAG-hyPBase plasmid. After 48 h, dual antibiotic selection with 200 μg/mL hygromycin and 5 μg/mL puromycin was applied for two weeks. Single-cell clones expressing BFP and GFP were sorted by flow cytometry and expanded for subsequent chromatin dynamic tracking experiments.

Single-molecule tracking (SMT) and data analysis of PCNA

To enable PCNA single-molecule tracking, target proteins were expressed as HaloTag fusion proteins in stable cell lines generated as described earlier. HeLa cells were synchronized at the G1/S transition and labeled with the fluorescent dye JF549 (10 μM, diluted 1:1000 in DMEM containing aphidicolin at 2 μg/mL, Sigma-Aldrich, A0781). The cells were incubated at 37°C for 20 min to allow the dye to bind to the HaloTag fusion proteins. After labeling, the unbound dye was removed by washing the cells three times with PBS containing aphidicolin. The cells were then transferred to phenol red-free DMEM (also containing aphidicolin) for imaging. The presence of aphidicolin ensured that cells remained in the G1/S transition during the labeling and imaging processes. Single-molecule tracking was performed similarly to the previously described method,[98] using a Nikon N-STORM microscope equipped with a 561 nm laser (2RU-VFL-P-300-488-B1R; MPB) and total internal reflection fluorescence (TIRF) capability. The microscope was adjusted to high-inclined laminated optical sheet (HILO) illumination to reduce nuclear background and enhance signal quality. Initial widefield fluorescence imaging was conducted to locate cells in the appropriate phase. After selecting appropriate cells, 100 frames of widefield images were captured with a split laser intensity set as 1%. For single-molecule tracking, the split laser intensity was increased to 100% (laser power ∼35 mW), with an exposure time of 20 ms. Rapid photobleaching was performed for approximately 30 s to reduce background signals and sparsely label individual molecules suitable for tracking. Once the background was sufficiently reduced and the single-molecule signal was sparse, 10,000–20,000 frames of single-molecule images were captured.

The acquired single-molecule trajectories were analyzed using Fiji[85] with the TrackMate[86] plugin. Single molecules were automatically detected and tracked using the Laplacian of Gaussian (LoG) detector. Parameters were adjusted to accurately detect molecules while excluding noise. TrackMate was used to process the image sequences and output single-molecule trajectories. The resulting trajectory data were exported to custom MATLAB scripts for further analysis. Each individual MSD curve was fitted by least-squares regression to the following model.

$$MSD = 4Dt^{\alpha}$$

Diffusion coefficients (D) and anomalous diffusion exponents (α) were calculated to quantify the molecules' movement. The diffusion coefficient was estimated by measuring the mean squared displacement (MSD) of molecules over time, representing their mobility. The anomalous diffusion exponent was used to assess deviations from Brownian motion.

Chromatin loci dynamic tracking

Chromatin loci dynamic tracking was adapted from previously described methods.[97] WT and Lamin A/C KO HeLa cells were transfected with sgRNA expression plasmids described above targeting the same genomic loci as in previous work.[97] After 24–48 h of culture, cells were prepared for imaging.

Dynamic tracking experiments were conducted on a Nikon N-STORM microscope with a 488 nm laser (2RU-VFL-P-300-488-B1R; MPB) to excite the sfGFP fluorophore. For chromatin loci dynamic tracking, the laser power was set to 10 μW, and images were acquired with 100 ms exposure time. Cells were maintained at 37°C and 5% CO_2 in a stage-top incubation chamber to ensure viability during live-cell imaging. The further analysis was consistent with PCNA single molecular tracking.

Confocal and STED microscopy imaging and data analysis

Confocal and STED imaging were performed using the Stedycon system (Abberior) equipped with a 100× oil-immersion objective (UPlanSApo 100×, 1.40 NA, Olympus) for high-resolution imaging. HeLa cells were seeded onto glass-bottom dishes and synchronized as described in the article. Immunofluorescence staining was performed, with or without prior EdU labeling, depending on the description in the Main. EdU labeling, where applicable, was achieved via click chemistry using the SIR dye. Specifically, STAR Orange (Abberior) and STAR Red (Abberior) dyes were used for STED immunofluorescence staining, corresponding to the green and magenta markers in the figure, respectively. Prior to imaging, samples were washed three times with ultrapure water

and air-dried overnight, followed by mounting with an appropriate mounting medium. The mounted samples were stored at −20°C until imaging.

During imaging, the samples were positioned on the stage, and the focus and target cells were carefully adjusted to ensure optimal clarity in all channels. For STED, a 775 nm depletion laser was used in combination with either a 647 nm or 561 nm excitation laser, depending on the fluorophore, to capture confocal images. Key imaging parameters were optimized, and the system's software was adjusted to achieve the best resolution and signal-to-noise ratio. The specific imaging parameters used in this experiment are detailed as follows: Replication sites (EdU, 10 min) and RDs (BrdU, 45 min) were visualized in the 647 nm channel with an STED laser intensity of 30% and a scan number of 5. Lamin A/C was also imaged in the 647 nm channel with an STED laser intensity of 40% and a scan number of 5. PCNA, CTCF, and pH2AX were imaged in the 561 nm channel with STED laser intensities of 60%, 60%, and 70%, respectively, and each with a scan number of 5. STED imaging was carried out with appropriate adjustments to the excitation and depletion laser intensities to minimize photobleaching while maintaining high-resolution signal capture.

STED images were deconvolved using Huygens Professional software (Scientific Volume Imaging, https://svi.nl/Huygens-Professional). System-adaptive parameters provided by the software were used to ensure accurate deconvolution while preserving the authenticity of the raw data. Deconvolved images were converted into TIFF format. The TIFF images (including confocal and STED) were analyzed using custom-developed code to identify and quantify specific biological structures. The analysis pipeline first involved the identification of nuclei using morphological algorithms that delineate the core regions of cells. Adaptive thresholding was then applied to segment protein clusters and replication signals. Several key parameters were computed to assess the features and spatial distribution of protein clusters within the cells: mean fluorescence intensity, cluster count, size, area, NND, and barycenter distance. The barycenter distance was defined as the spatial barycenter distance between the early replication sites and the RD, normalized by the RD's radius. To ensure accurate assignment, an early replication site was analyzed only if its spatial barycenter distance to the nearest RD was shorter than half of the RD's major axis length.

Expansion Microscopy (ExM) imaging and data analysis

HeLa cells were seeded onto coverslips and synchronized, followed by 45-min EdU incorporation, click chemistry with dye SIR, and immunofluorescence for PCNA with dye AF594, as previously described. The ExM protocol was then adapted from the methods outlined by Shi et al.[35]

Following the sample preparation, cells were post-fixed in a solution containing 3% PFA and 0.1% glutaraldehyde (GA) in PBS for 15 min at room temperature with gentle shaking. This fixation buffer was freshly prepared by dissolving 4 g of PFA in 50 mL of water, heated to 60°C to assist dissolution, and adjusted to a pH of 7.0–7.4.

The cells were washed three times in PBS (5 min per wash), followed by a second fixation step using 0.7% PFA and 1% acrylamide (AaM) in 1× PBS at 37°C for 1–6 h. This step ensured the direct anchoring of proteins and DNA into the first layer of hydrogel. Cells were then incubated in a pre-gel solution composed of 19% sodium acrylate (SA), 10% acrylamide (AAm), 0.1% N,N′-methylenebisacrylamide (DHEBA), 0.25% TEMED, and 0.25% ammonium persulfate (APS). Cells were embedded by covering them with the gel mixture, allowing polymerization at room temperature for 15 min, followed by 1.5 h in a humidified 37°C incubator.

The hydrogel was denatured in a solution containing 200 mM SDS, 100 mM NaCl, and 50 mM Tris (pH 6.8) for 15 min at room temperature, followed by incubation at 73°C for 1 h. After denaturation, the hydrogel was transferred to a dish containing deionized water for the expansion phase. Water was replaced twice, with 1-h intervals, and then the gel was allowed to expand overnight at room temperature. The final hydrogel diameter reached approximately 4 cm, ensuring optimal sample expansion.

The following imaging acquisitions were performed using the Dragonfly confocal imaging system. Gel samples were imaged with a 60× oil-immersion objective (1.6 NA). Multi-channel images were acquired sequentially. The resulting TIFF images were analyzed using custom-developed code, previously applied to STED imaging, to identify and quantify the distribution of PCNA and RD.

STORM imaging and data analysis

The STORM imaging and analysis were adapted from our previous work.[33] HeLa cells were seeded onto glass-bottom dishes and synchronized as previously described, followed by click chemistry for EdU with dye AF647, and immunofluorescence for BrdU with dye Cy3B.

STORM imaging was conducted using a custom-built inverted microscope (IX83, Olympus) configured for widefield excitation. The system was equipped with a 100×, 1.49 NA oil-immersion objective lens (U APO N, Olympus). A multiband dichroic mirror (Chroma) was used to reflect the excitation lasers while allowing the transmission of emitted fluorescence. Additional emission filters (Chroma) were applied to isolate fluorescence signals from individual channels. Images were acquired on an EMCCD camera (Ixon Ultra EMCCD, Andor) with a resolution of 512*512 pixels (115 nm per pixel). A near-infrared laser was utilized to maintain precise focus during acquisition.

TetraSpeck Microspheres (0.1 μm in diameter, Thermo, T7279) were incubated with the sample at a 1:50000 ratio for 1 h, followed by three washes with PBS to remove non-adherent beads. Imaging was performed in a buffer composed of 10% (w/v) glucose, 20 mM NaCl, 100 mM Tris-HCl, 600 μg/mL glucose oxidase, 60 μg/mL catalase, and 1% (v/v) β-mercaptoethanol. Fluorophores were activated with a 405-nm laser (OBIS, Coherent) and excited using 561-nm and 647-nm lasers (MBP Communications), depending on the channel. The laser power densities at the sample plane were 1 kW/cm^2 for the 647 nm laser and 2 kW/cm^2 for the 561 nm laser.

STORM imaging data were acquired with a 30-ms exposure time per frame, generating a total of 60,000 frames for each channel (561 nm and 647 nm). After imaging, the STORM buffer was removed by washing the samples three times with PBS, and the samples were stored in PBS at 4°C shortly.

For the analysis of single-molecule localizations, the target cells and TetraSpeck Microspheres were first manually selected from the acquired images. Channel correction and drift correction were carried out using ThunderSTORM[87] by aligning the positions of the microspheres. Following drift correction, single-molecule reconstructions and channel filtering were performed independently for the 647 nm and 561 nm channels using ThunderSTORM.

For spatial clustering, SR-Tesseler[88] was employed for threshold-based segmentation of the processed images. A Voronoi diagram was constructed for each channel, with the 561 nm channel used to define RDs and the 647 nm channel for early replication sites. Clustering was performed by applying appropriate density factors, with a density factor of 0.5 for defining RDs in the 561 nm channel, and a density factor of 5 for identifying replication sites in the 647 nm channel. The identified clusters were analyzed by calculating key spatial features, including the number of clusters and the diameter of each cluster.

QUANTIFICATION AND STATISTICAL ANALYSIS

Statistical analyses were conducted using GraphPad Prism software (version 9). Unless otherwise specified, an unpaired two-sample parametric *t* test was utilized to assess significance levels, denoted as: $^{****}p < 0.0001$, $^{***}p < 0.0005$, $^{**}p < 0.01$, $^{*}p < 0.05$; ns, not significant. In scatterplots, horizontal lines represent mean values, with error bars indicating ±standard deviation (s.d.). For violin or boxplots, the central line represents the median, while the upper and lower bounds of the box indicate the 25th and 75th percentiles, respectively. Whiskers extend to data points within 1.5× the interquartile range of the box limits.